

1
2
3
4
5
6
7
8
9
10
11
12
13
14
15
16
17
18
19
20
21
22
23
24
25
26
27
28
29
30
31
32
33
34
35
36
37
38
39
40
41
42
43

**Observations of Shoaling Internal Wave Transformation Over a Gentle Slope in
the South China Sea**

Steven R. Ramp¹, Yiing Jang Yang², Ching-Sang Chiu³, D. Benjamin Reeder³, and
Frederick L. Bahr⁴

Last modified April 14, 2022
Submitted to: Nonlinear Processes in Geophysics

[1] {Soliton Ocean Services LLC, Falmouth, MA 02540}
[2] {Institute of Oceanography, National Taiwan University, Taipei, Taiwan}
[3] {Dept. of Oceanography, Naval Postgraduate School, Monterey, CA 93943}
[4] {Monterey Bay Aquarium Research Institute, Moss Landing, CA 95039}
Correspondence to: S. R. Ramp (sramp@solitonocean.com)

44 **Abstract**

45

46 Four oceanographic moorings were deployed across the South China Sea
47 continental slope near 21.85°N, 117.71°E, from May 30 to July 18, 2014 for the
48 purpose of observing high-frequency nonlinear internal waves (NLIWs) as they
49 shoaled across a rough, gently sloping bottom. Individual waves required just two
50 hours to traverse the array and could thus easily be tracked from mooring-to-
51 mooring. In general, the amplitude of the incoming NLIWs tracked the fortnightly
52 tidal envelope in the Luzon Strait, lagged by 48.5 hours, but were smaller than the
53 waves previously observed to the southwest near the Dongsha Plateau. The type a-
54 waves and b-waves were observed, with the b-waves always leading the a-waves by
55 6-8 hours. Most of the NLIWs were remotely generated, but a few of the b-waves
56 formed locally via convergence and breaking at the leading edge of the upslope-
57 propagating internal tide. Waves incident upon the moored array with amplitude
58 less than 50 m and energy less than 100 MJ m^{-1} propagated adiabatically upslope
59 with little change of form. Larger waves formed packets via wave dispersion. For
60 the larger waves, the kinetic energy flux decreased sharply upslope between 342 m
61 to 266 m while the potential energy flux increased slightly, causing an increasing
62 ratio of potential-to-kinetic energy as the waves shoaled. None of the waves met the
63 criteria for convective breaking. The results are in rough agreement with recent
64 theory and numerical simulations of shoaling waves.

65

66

67

68 **1 Introduction**

69 Considerable field work has now been dedicated to observing and understanding
70 the very large amplitude, high-frequency nonlinear internal waves (NLIW) in the
71 northeastern South China Sea (SCS). It has now been well established that the
72 waves emerge from the internal tide which is generated by the flux of the barotropic
73 tide across the two ridges in the Luzon Strait [Buijsman et al., 2010a, 2010b; Zhang
74 et al., 2011]. Both tidal conversion and dissipation are high around the ridges
75 [Alford et al., 2011], but adequate energy survives to escape the ridges and
76 propagate WNW across the sea. As they do so, the internal tides steepen nonlinearly
77 until eventually the NLIW are formed [Farmer et al., 2009; Li and Farmer, 2011;
78 Alford et al., 2015; Chang et al., 2021a]. The longitude where this takes place
79 depends on the details of the forcing and stratification but based on satellite
80 imagery it is not until at least $120^{\circ} 30'E$, roughly 50 km west of the western (Heng-
81 Chun) ridge [Jackson, 2009]. This longitude is hypothesized to be the minimum
82 distance/time required for the internal tide to nonlinearly steepen and break, or
83 perhaps the first point where tidal beams intersect the sea surface west of the
84 western ridge. Once the NLIW have formed, they propagate WNW across the deep
85 SCS basin with remarkably little change of form [Alford et al., 2010; Ramp et al.,
86 2010]. Once the waves start to shoal on the continental slope however, roughly
87 between 1000m to 150m depth, the changes become quite dramatic. Wave
88 refraction due to the shallower depth and changing stratification tends to align the
89 wave crests with the local topography. Incident NLIWs which were initially solitary
90 may form packets via wave breaking or dispersion [Vlasenko and Hutter, 2002;
91 Vlasenko and Stashchuk, 2007; Lamb and Warn-Varnas, 2015]. Some very large
92 waves may split into two smaller waves [Small 2001a, 2001b; Ramp, 2004]. When
93 the wave's orbital velocity exceeds the propagation speed, usually between 300m -
94 150m depth, the largest waves may break and form trapped cores that transport
95 mass and nutrients onshore [Farmer et al., 2011; Lien et al., 2012, 2014; Rivera-
96 Rosario et al., 2020; Chang et al., 2021b]. Still farther onshore where the upper
97 layer thickness exceeds the lower, the depression waves are transformed into
98 elevation waves [Orr and Mignerey, 2003; Duda et al., 2004; Ramp et al., 2004; Liu et
99 al., 2004]. The elevation waves presumably continue propagating WNW towards
100 shore and dissipate in shallow water, but observations to the west of this point are
101 scarce.

102
103 Two types of NLIWs, called a-waves and b-waves, have been repeatedly observed, a
104 parlance first coined by Ramp et al. [2004]. Based on the Asian Seas International
105 Acoustics Experiment (ASIAEX) results, the a-waves consisted of rank-ordered
106 packets that arrived at the same time every day and were generally larger than the
107 b-waves, which were usually solitary and arrived one hour later each day. It has
108 subsequently been shown via longer data sets that the timing is not universal, and
109 that b-waves may sometimes be larger than a-waves [Alford et al., 2010; Ramp et al.,
110 2010]. It is now recognized that the a-waves are generated in the southern portion
111 of the Luzon Strait and the b-waves to the north [Du et al., 2008; Zhang et al., 2011;
112 Ramp et al., 2019]. The b-waves are subject to massive dissipation over the shallow

113 northern portion of the western (Heng-Chun) ridge [Alford et al., 2011] but the a-
114 waves are not. The distinction matters because the energy and propagation
115 direction of the trans-basin waves incident on the continental slope determines how
116 they behave as they shoal. These differences are explored further in this paper.
117

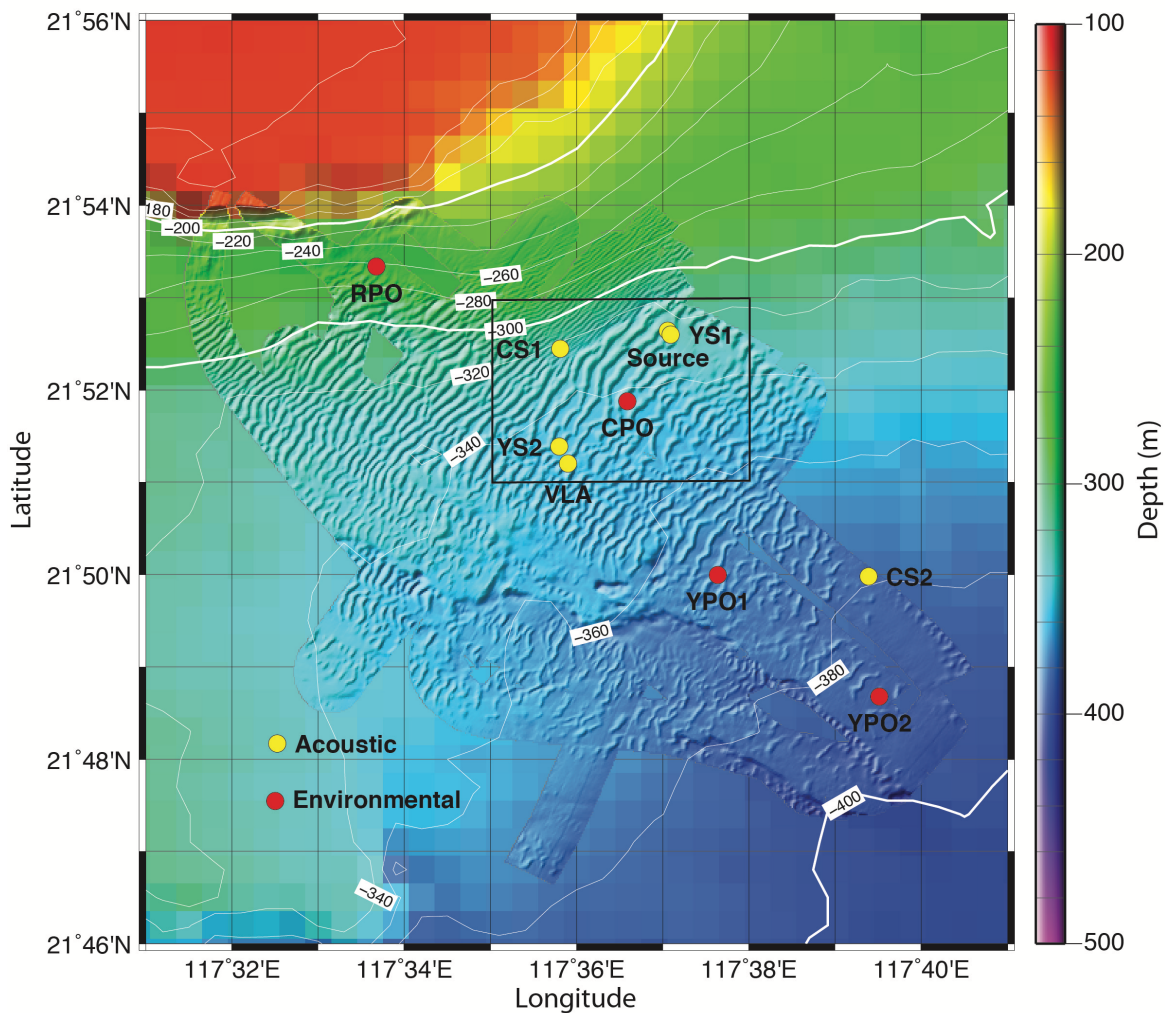
118 The present study was motivated by the discovery of large ($h > 15\text{m}$, λ order 350m)
119 undersea sand dunes on the sea floor along a transect southeastward from 21.93°N,
120 117.53°E in the northeastern South China Sea [Reeder et al., 2011]. Subsequent
121 multi-beam echo surveys (MBES) during 2013 and 2014 revealed that the dunes
122 occupy at least the region spanning 21.8 to 21.9°N and 117.5 to 117.7°E (Figure 1).
123 This region is on the continental slope slightly northeast of the Dongsha Plateau.
124 The bottom slope in the dunes region is relatively slight with respect to steeper
125 bottom slopes progressing both offshore and onshore from the dune field. The sand
126 dunes are of interest due to their impact on shallow-water acoustic propagation,
127 and their interaction with shoaling internal tides and NLIWs traveling WNW up the
128 slope. The acoustic issues are addressed in other papers emerging from the
129 program [Chiu and Reeder, 2013; Chiu et al., 2015]. Oceanographic questions of
130 interest include: 1) How are NLIWs transformed as they shoal over a gentle slope
131 between 388m and 266m over the continental slope? 2) What are the physical
132 mechanisms responsible for this transformation? and 3) How does the increased
133 bottom roughness in the dune field affect energy dissipation in the shoaling internal
134 tides and NLIWs, relative to other locations? Geophysical problems of interest
135 include: 4) What, if any, is the role of the NLIW in sediment re-suspension and dune
136 building? 5) What determines the spatial scales of the dunes? and 6) Why are the
137 dunes located where they are, and why are they not observed elsewhere?
138

139 This paper addresses how the high-frequency nonlinear internal waves were
140 transformed under shoaling, while the NLIW dissipation and role in the dune-
141 building process will be addressed in separate works [Helfrich et al., 2022]. The
142 data and methods are described in section 2, the NLIW arrival patterns and their
143 relation to the source tides in section 3, and the wave transformations and energy
144 conservation in section 4. A summary and conclusion section follows.
145

146 **2 Data and Methods**

147

148 An array of four oceanographic moorings were deployed across the continental
149 slope from 21.81°N, 117.86°E (386 m) to 21.89°N, 117.56°E (266 m) during May 31
150 to June 18, 2014 (Figure 1, Appendix A). The moorings labeled YPO2, YPO1, CPO,
151 and RPO were separated by 4.10, 3.30, and 5.69 km respectively corresponding to
152 wave travel times of 36.5, 30.3, and 56 min between moorings. Temperature and
153 salinity were sampled at 60s intervals. Instrument spacing ranged from 15 m to a
154 maximum of 30 m in the vertical to resolve internal wave amplitudes. Currents at
155 RPO were sampled using three downward looking 300 kHz ADCPs moored at 27 m,
156 105 m, and 184 m depth which provided coverage of the entire water column except
157 the upper 20 m. Currents at CPO were also sampled using three 300 kHz ADCPs, one



158
159

160 *Figure 1. Locator map for the Sand Dunes 2014 field experiment. This paper primarily*
 161 *concerns the environmental moorings indicated by the red dots, although temperature*
 162 *from the “source” mooring is also used. The area within the black box is expanded in*
 163 *Figure 2.*

164

165 downward-looking unit moored at 15 m depth, and an up/down pair at 264 m
 166 depth. Since the range of these instruments was nominally 100 m, there was an
 167 unsampled region spanning roughly 115 – 164 m depth at mooring CPO. Currents at
 168 YPO1 and YPO2 were sampled using one 75 kHz and one 300 kHz ADCP. The 75
 169 kHz instruments were mounted downward looking in the top syntactic foam sphere
 170 at 20 m depth. The 300 kHz instruments were also mounted downward looking in
 171 cages at 300 m depth. The 300 kHz instruments burst-sampled for 20 s every 90 s,
 172 while the 75 kHz instruments sampled once per second and were averaged to 90 s
 173 intervals during post-processing. These sampling rates were adequate to observe
 174 the shoaling NLIWs with no aliasing. A fifth mooring labeled “source” on roughly
 175 the same isobath as CPO (Figure 1) sampled temperature only from 27 to 267 m.

176 This mooring was targeted for the same “trough” in the sand dune field as CPO to
177 examine along-crest acoustic propagation. It additionally proved useful to identify
178 the precise phasing and orientation of the internal wave crests in the along-slope
179 direction.

180

181 **3 Results**

182

183 *3.1 The Nature of the Dunes*

184

185 The stage is set by a zoomed-in view of the study region showing the seafloor sand
186 dunes as depicted by the MBES data (Figure 2). A change in the bottom slope forms
187 a very clear line of demarcation between lower (4 m) dunes with shorter (100 m)
188 wavelength and the larger (10-15 m) dunes with longer (260 m) wavelength. Dunes
189 in these regions were nearly sinusoidal. Farther down the slope in water > 360m
190 depth, the dunes were “parted” meaning the trough widths were much greater than
191 the crest widths. Mooring RPO was located in the first region with steeper slope,
192 CPO was in the second region of smaller slope and large sinusoidal dunes, and
193 moorings YPO1 and YPO2 were in a region with similar mean bottom slope but
194 parted dunes. Repeat MBES surveys indicated that during 2013-14, the dunes were
195 stationary to within the accuracy of the surveys. For purposes of this paper, the
196 most important fact about the bottom is the sharp, clear change of bottom slope
197 across the white dotted line (Figure 2) from $1:35 = .03 = 3\% = 2.0^\circ$ over the
198 shallower part to $1:160 = .006 = 0.6\% = 0.3^\circ$ over the deeper part. These slopes are
199 essential for comparing the observations to theory.

200

201

202

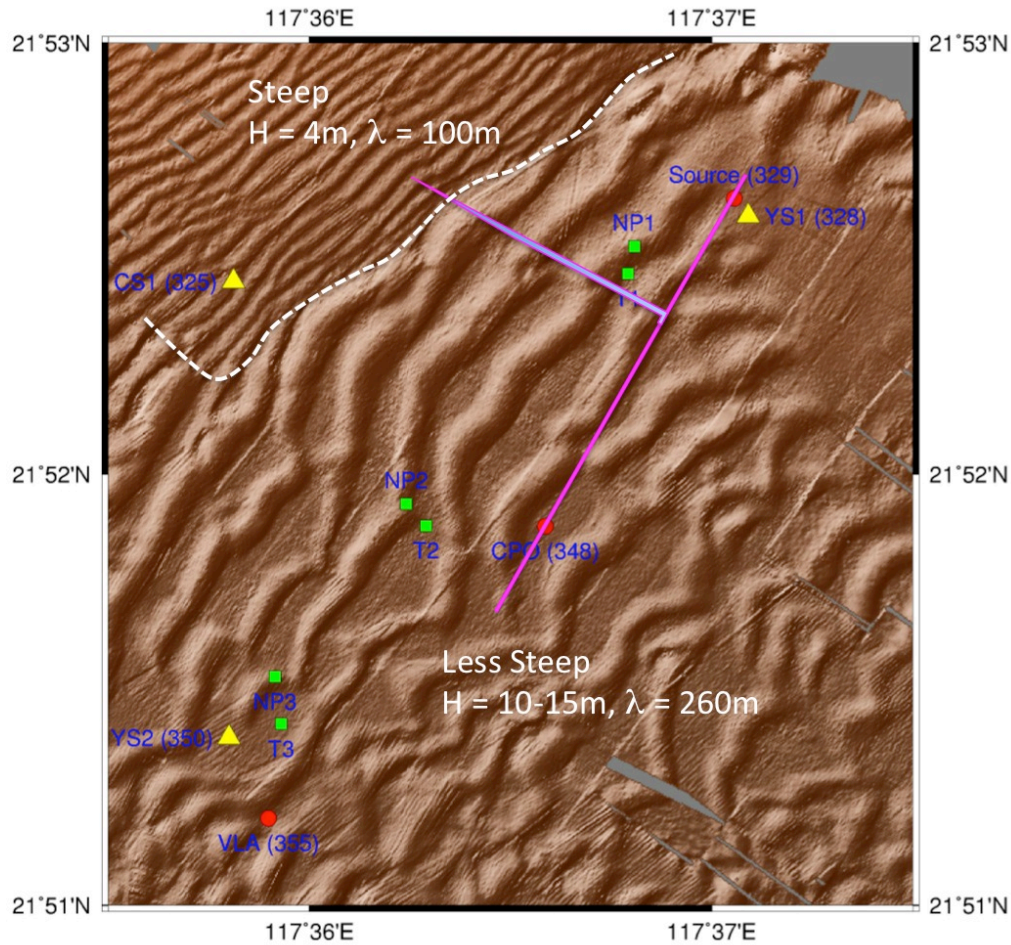
203 *3.2 Wave Arrival Patterns*

204

205 While fine-tuning the NLIW generation problem is beyond the scope of this paper, the
206 fundamental properties of the wave arrival patterns can be understood via comparisons
207 with the generating tide in the Luzon Strait. Having no remote observations during
208 spring 2014, the wave arrival patterns at the sand dunes moored array were compared
209 with the barotropic tidal forcing in the Luzon Strait as obtained from the TPXO7.0 global
210 tidal model [Egbert and Erofeeva, 2002]. The model output has been shown to be in
211 good agreement with the limited observations available in the Luzon Strait [Ramp et al.,
212 2010] and is thus a good indication of the tidal amplitude and phase at generation.

213

214 To begin, all the NLIWs arriving at the moored array were identified using large-scale
215 plots of temperature, salinity, and velocity. The arrivals were then summarized for the
216 entire time series by labeling the displacement of the 20°C isotherm from its mean
217 position at mooring RPO (Figure 3, top). The wave arrivals, as indicated by sharp
218 downward displacements of the isotherm, fall into two groups or “clusters” of waves each
219 within a fortnightly envelope. The waves were labeled using previous conventions, using
220 lowercase a- and b- for the first cluster and uppercase A- and B- for the second for
221 uniqueness. This nomenclature will be used to refer to individual waves subsequently.



223

224

225

226 *Figure 2. The sea floor in the study region as observed by a multi-beam echo sounder*

227 *(MBES) survey during June 2014. The region is delineated by the black box in Figure 1.*

228 *The dotted white line indicates a sharp change in bottom slope, steeper towards the*

229 *northwest. The magenta arrow indicates the direction of propagation of the nonlinear*

230 *internal waves (NLIW) as determined by wave arrival times at moorings CPO and*

231 *“source” (pink line).*

232

233 There is no dynamical difference implied by the upper- vs. lowercase names. A total of

234 21 NLIWs with amplitude greater than 20 m were observed, 13 a-waves and 8 b-waves.

235 When b-waves were present, the waves arrived in b- and a- pairs with the b-wave always

236 leading the a-wave by on average 6.6 hours. The a-waves began arriving earlier in the

237 fortnightly cycle for instance 6/7 to 6/11. The b-waves began arriving later and grew

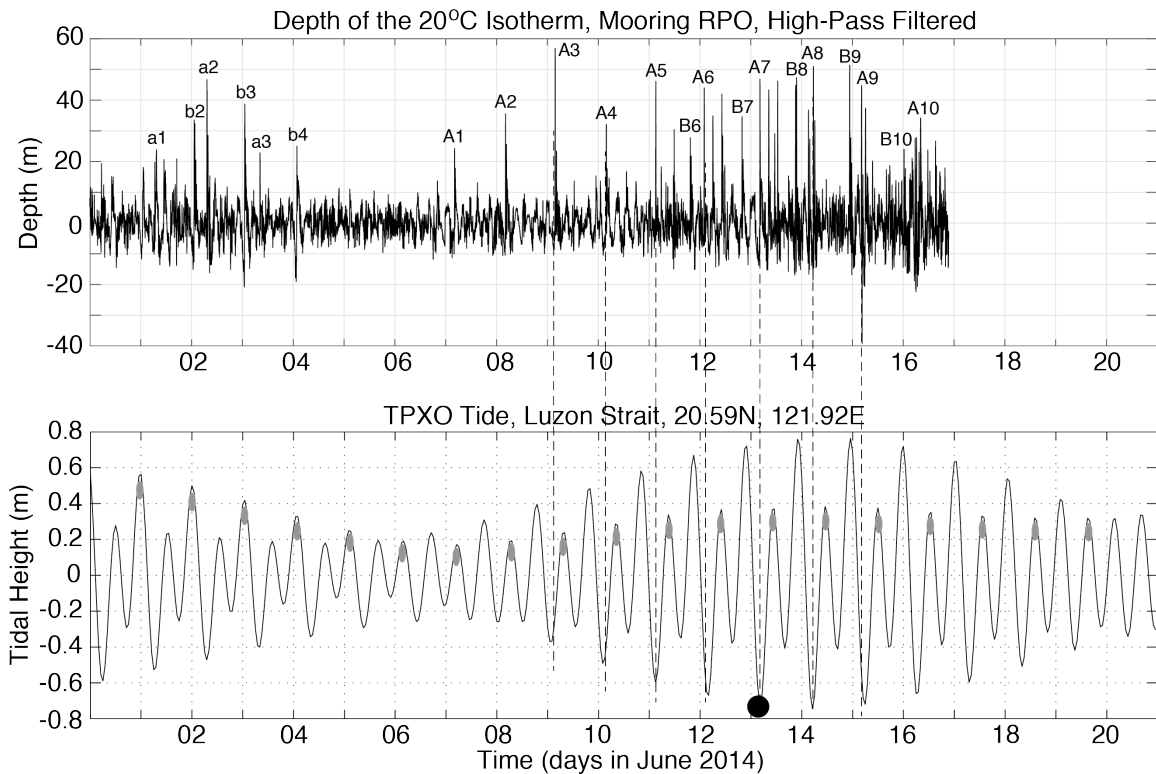
238 larger later in the fortnightly cycle. With the exception of 6/3 and 6/15, the a-waves were

239 larger than the b-waves.

240

241 The RPO wave amplitude time series was then plotted over the Luzon Strait tides (Figure

242 3, bottom) with the wave amplitudes lagged back by the propagation time from the



244

245

246

247 *Figure 3. (Top) Time series showing the depth of the 20°C isotherm observed by*
 248 *mooring RPO located at the 266 m isobath (Figure 1). The time series was high pass*
 249 *filtered to separate thermal displacements due to NLIWs from the internal tides and*
 250 *mean (mesoscale and seasonal) flows. The sharp depressions of the isotherm indicate*
 251 *passing NLIWs. The type-a and type-b waves are labeled using lower case for the first*
 252 *fortnight and upper case for the second. (Bottom) Tidal amplitude in the central*
 253 *Luzon Strait from the TPXO global tidal model [Egbert and Erofeeva, 2002], at a point*
 254 *located between Batan and Itbayat Island in the Luzon Strait. The gray ellipses*
 255 *indicate how the major and minor tidal beats switched positions during the neap tide.*
 256 *The black circle indicates the time of the full moon on June 13th. The waves (top panel)*
 257 *have been lagged back by the propagation time from the strait (48.5 hours) to better*
 258 *align with the barotropic tidal envelope in the generating region. The vertical dashed*
 259 *lines show how the lagged a-waves aligned with the ebb tide in the straits.*

260

261

262 source to the mooring. The lag time (48.5 hours) was estimated by making a small
 263 adjustment to the propagation time nearby (50.3 hours) which was calculated using a full
 264 year's data [Ramp et al., 2010]. Several obvious results emerge from this comparison.
 265 First, the NLIW amplitudes at RPO track the fortnightly tidal amplitudes in the Luzon
 266 Strait. The largest waves were generated at spring tide in the strait and no waves at all
 267 were generated during neap. This result is consistent with longer (11 month) time series
 268 obtained over the continental slope to the southwest [Chang et al., 2021a]. Second, the

269 generating tide was mixed, diurnal dominant, with a strong diurnal variation, but only the
270 major beats resulted in NLIWs in the far field. The minor beats and the neap tides were
271 apparently too weak to spawn NLIWs downstream. As a result, just one wave of each
272 type was generated per day, despite the generating tide being semidiurnal. The major and
273 minor beats switched positions during the neap tide, and the wave arrivals at the sand
274 dunes array switched positions accordingly. Third, the lagged a-waves aligned precisely
275 with the major ebb (eastward) tide in the Luzon Strait, in agreement with previous work.
276 This suggests generation by the lee wave mechanism [Buijsman et al., 2010a]. Finally,
277 the b-waves were sometimes aligned well with the major flood tide preceding each a-
278 wave, but we now believe this to be coincidence: The directional histograms (not shown)
279 show the a-waves on average traveling along a path about 24 degrees more northward
280 (294°) than the b-waves (270°), consistent with the primary source for the a-waves being
281 located farther to the south along the Luzon ridge system. The b-waves lead because
282 their generation site was closer to our observation point on the Chinese continental slope.
283

284 One example of the daily moored temperature time series at mooring RPO is shown to
285 further illustrate these results (Figure 4). During June 9 to 13, the A-waves arrived at
286 about the same time each day while from June 14-18, they arrived about an hour later
287 each day. This result, that the A-wave arrival times were constant early in the fortnightly
288 tidal cycle but delayed an hour per day as the waves increased in amplitude later in the
289 cycle was consistent with the model results of [Chen et al., 2013]. Wave A7 on June 15
290 was anomalously late by about 2 hours relative to waves A6 and A8. This is attributed
291 to the passing of tropical storm Hagabus on June 14-15 with accompanying strong wind-
292 forced currents and upper ocean mixing. The B-wave arrivals began at about 20:00 on
293 June 13, and were subsequently delayed about an hour per day, similar to the
294 corresponding A-waves (Figure 4). The difference in the arrival times between the B-
295 waves and the A-waves was 6:30, 8:25, 6:15, and 5:50 on June 14-17 respectively. Wave
296 B7 was not delayed by the storm, which provides further evidence for different
297 propagation paths for the B-waves vs. the A-waves. On June 16-18 two A-waves of near
298 equal amplitude arrived about 2 hours apart. These “double A-waves” appeared over the
299 slope only near spring tide in the Luzon Straits, and the second one has been designated
300 by a prime. The origin of these waves is unclear. We speculate that the new A' waves
301 originated from a different (third) source in the Luzon Straits that is only active under
302 maximum barotropic forcing. More observations in the source region are needed to
303 understand the wave generation issues, including this double a-wave phenomenon.
304

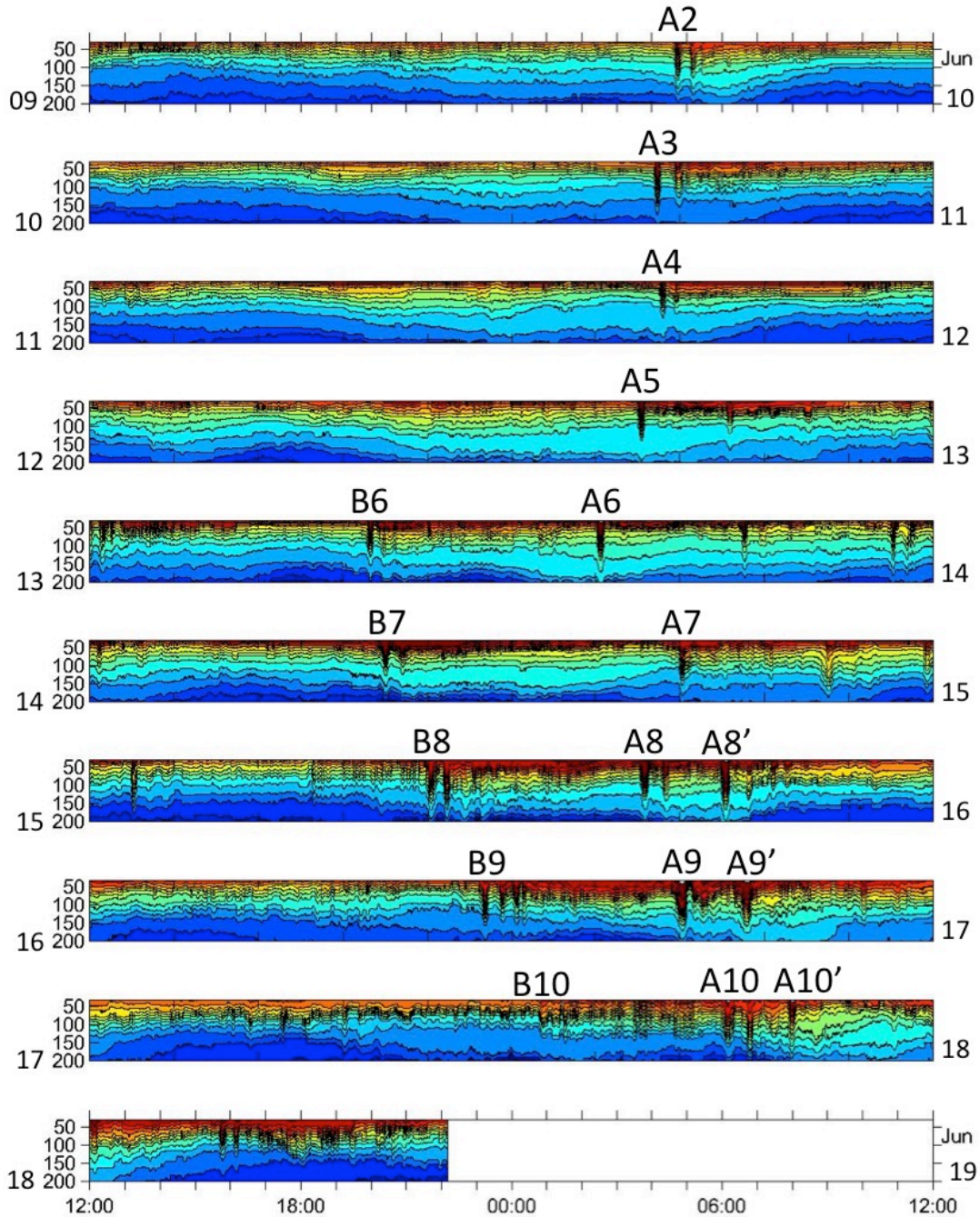
306 *3.3 Wave Transformation Over the Slope*

307
308 Many significant wave transformations were observed between the 386 m (YPO2)
309 and the 266 m (RPO) isobaths over the upper continental slope. Three sections of
310 the record are shown to illustrate different phenomena. The first sequence from
311 June 2 to 6 (Figure 5) evolved out of moderate and decreasing forcing in the Luzon
312 Strait (Figure 3). The observations captured the local steepening and breaking of
313 the tidal front to form b-waves as it shoaled. The internal tides at YPO2 were
314 diurnal and nearly sinusoidal with an amplitude of about 4°C (blue line). The a-

315 waves were already evident at YPO2, but not the b-waves. Then, beginning at YPO1
316 and continuing to CPO, the leading edge of the tidal front became very steep with a
317 temperature change of $1^{\circ}\text{C} / \text{min}$ for 5 minutes at CPO (black ellipses in Figure 5).
318 This front subsequently broke and formed b-wave packets b2 and b3 observed at
319 mooring RPO. This example thus demonstrates a local b-wave formation process
320 via steepening of the leading edge of the tidal front. This steepening temperature
321 front was due to velocity convergence at the head of the westward-propagating
322 internal tide. The formation of a similar bore-like feature at shallower depths (200
323 m – 120 m) was noted in the ASIAEX data [Duda et al., 2004] but they did not make
324 the connection to b-wave formation. Waves a1 and a2 lost amplitude and formed
325 packets as they shoaled between YPO2 and RPO. This process will be compared
326 with some recent theoretical ideas in the discussion section. Wave a3 was small at
327 YPO2 but gained amplitude as the tide progressed up the slope. This is because the
328 barotropic forcing in the Luzon Strait was weaker on June 5 than on June 2-4 (Figure
329 3). All the waves subsequently disappeared on June 7-8 during neap tide in the
330 Luzon Strait.

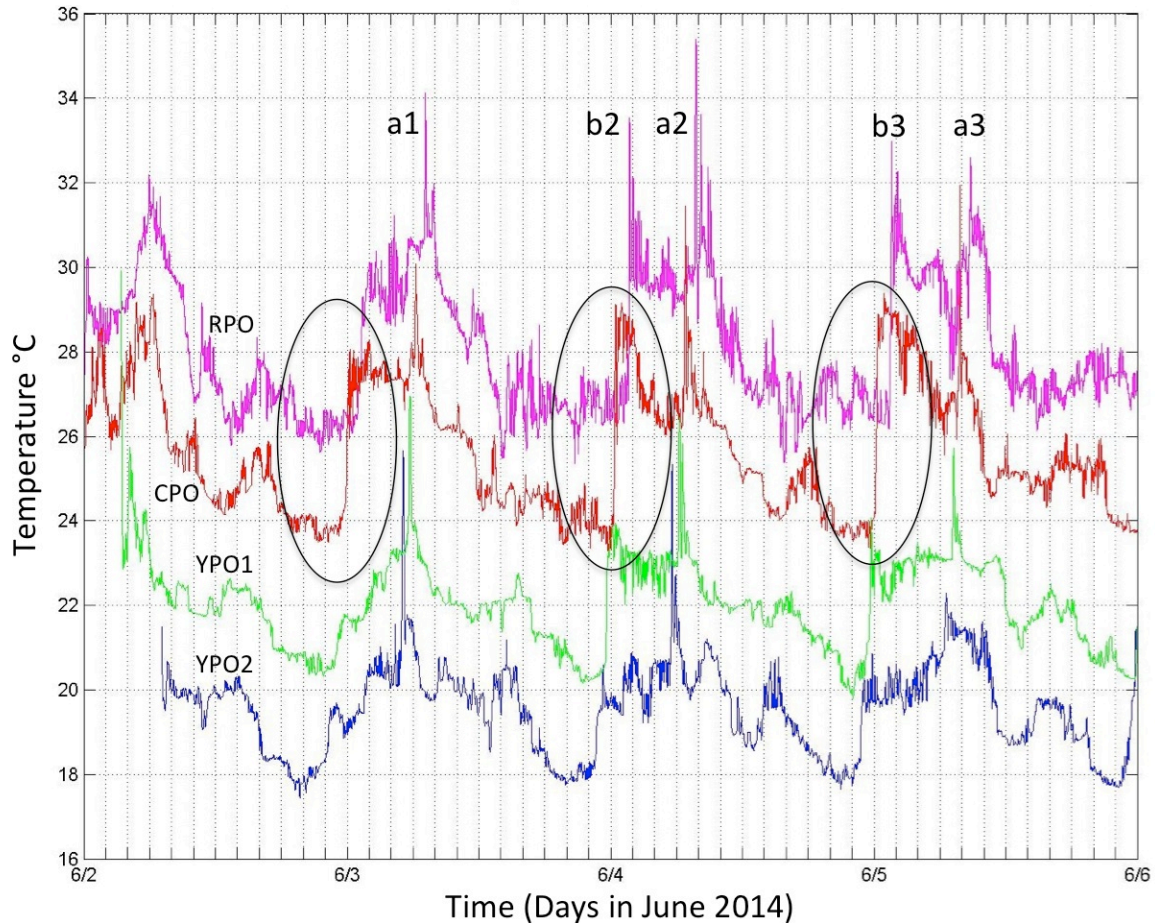
331
332 The second sequence during June 10-14 shows well developed A-wave packets
333 which originated from moderate but increasing remote forcing (Figure 6). Only A-
334 waves were observed until June 13 when the B-waves started to arrive. Wave B6
335 was weakly perceptible at YPO2 and increased in amplitude across the slope. The
336 temperature fluctuations induced by the A-waves increased across the slope and
337 reached a maximum of 7°C on June 11 at A3. The temperature gradients in the wave
338 fronts were again very steep, $1^{\circ}\text{C} / \text{min}$. The number of waves per packet increased
339 towards shallower water, most clearly in waves A2, A3, and A4. Two extraneous
340 solitary waves appeared trailing wave A5 on June 13 at CPO and RPO but were not
341 part of the A5 packet structure. Two similar waves appeared the next day trailing
342 wave A6 (Figure 7) and their origin is unclear.

343
344 The final sequence from June 14 to 18 was obtained during a period of maximal
345 forcing near spring tide at the source, and a very complicated field of NLIW emerged
346 (Figure 7). The B-waves were large and were evident at all the moorings. Wave B8
347 and B9 were solitary at YPO2 but had many waves per packet by the time they
348 reached RPO. The arrival timing was the same as the locally formed b-waves
349 (Figure 5) suggesting similar dynamics but faster/shorter development
350 time/distance when the forcing at the source was stronger. The A-waves continued
351 to grow at YPO2 during June 14-18. Interestingly, the temperature fluctuations due
352 to the largest waves did not increase monotonically as they traveled up the slope
353 from YPO2 to RPO. This is more clearly seen in a bar graph showing the maximum
354 amplitude of the isotherm of maximum displacement (Figure 8). Smaller waves
355 (June 9-12) gained amplitude as they shoaled. All waves larger than about 50 m
356



357
 358
 359
 360
 361
 362
 363
 364
 365
 366

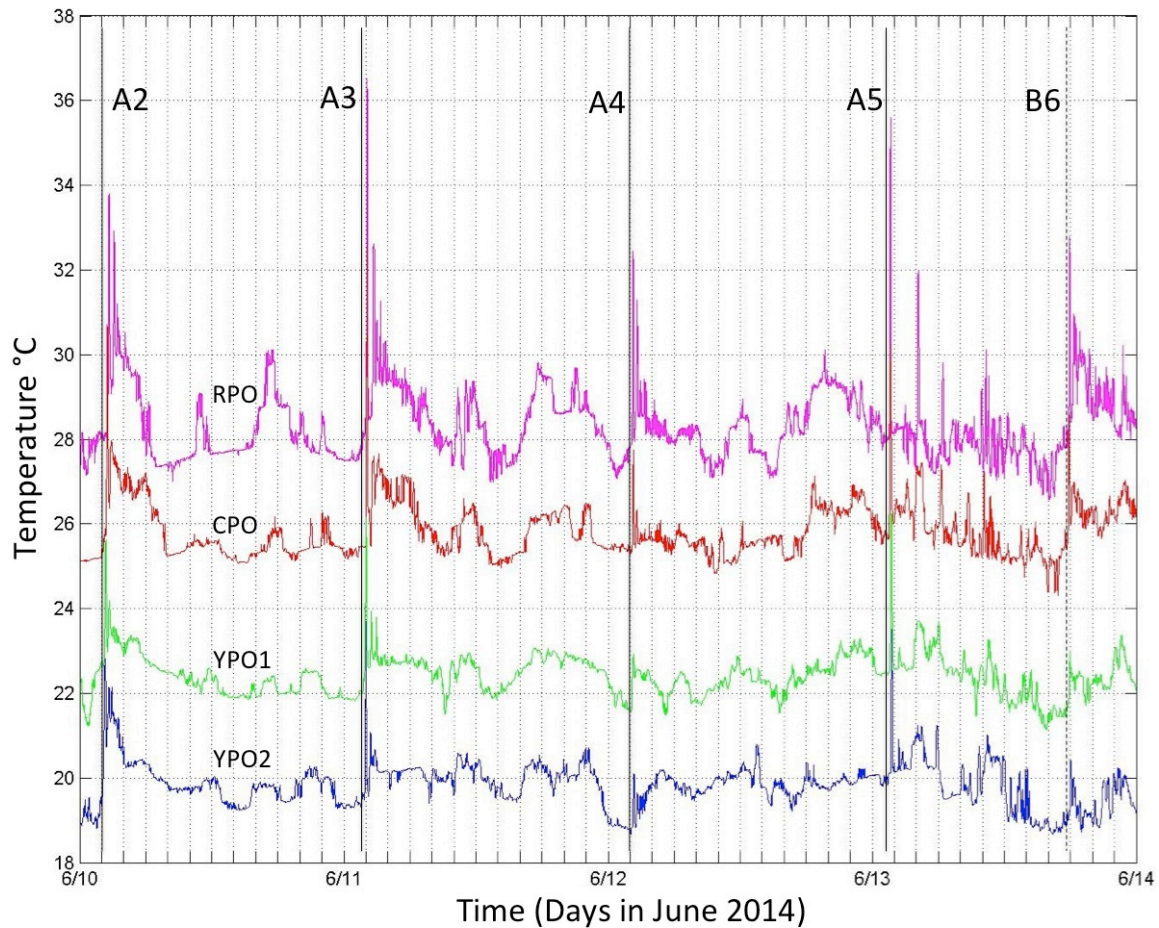
Figure 4. Temperature contour plots for mooring RPO from June 9 to 19, 2014. Each panel from top to bottom is one day centered on midnight, to capture both the A- and B-wave arrivals. The A-waves were prominent throughout this fortnightly cycle. The B-wave arrivals began on June 13, five days after the A-waves. The double A-waves (A8'-A10') arrived only during June 16-18. This and similar plots were used to label the waves in Figure 3.



367
368
369
370
371
372
373
374
375

Figure 5. Temperature vs. time during June 2-6 at all four moorings across the continental slope. The observations are from 75m, 79m, 97m, and 99m from moorings RPO, CPO, YPO1, and YPO2 respectively. Each time series has been offset vertically by 2 °C for clarity. The black ellipses highlight the region of strong temperature fronts at CPO that subsequently broke and formed b-waves at RPO.

376 offshore (June 13-18) lost amplitude as they shoaled, most clearly between CPO and
377 RPO, where the biggest change in bottom depth and slope occurred. This result is
378 consistent with the numerical results of [Lamb and Warn-Varnas, 2015] who also
379 found that smaller amplitude waves continued to gain amplitude into shallower
380 water but the larger waves did not. This fundamental result, that NLIW first gain
381 amplitude and then lose it as they shoal, is consistent with EKdV theory [Small,
382 2001; Vlasenko et al., 2005]. Note that all the wave amplitudes (Figure 8) were
383 smaller than those observed previously over the continental slope 44, 87, and 145
384 km to the southwest [Ramp et al., 2004; Lien et al., 2014; Chang et al., 2021a; Ramp
385 et al., 2022]. This is because, as seen in hundreds of satellite images (typified by
386 Figure 9), the NLIWs have maximum amplitude in the region just north of the
387 Dongsha Plateau near 20°N decreasing both northward and southward from there.
388 Along-slope observations have also shown a reduction in the upslope energy flux



390

391

392 *Figure 6. As in Figure 5, except during June 10-14, 2014. In this plot, the time series*
 393 *have additionally been shifted relative to YPO2 by the propagation time between*
 394 *moorings so that individual waves line up. The lag times used are 36.5 min for YPO1,*
 395 *66.8 min for CPO, and 122.8 min for RPO.*

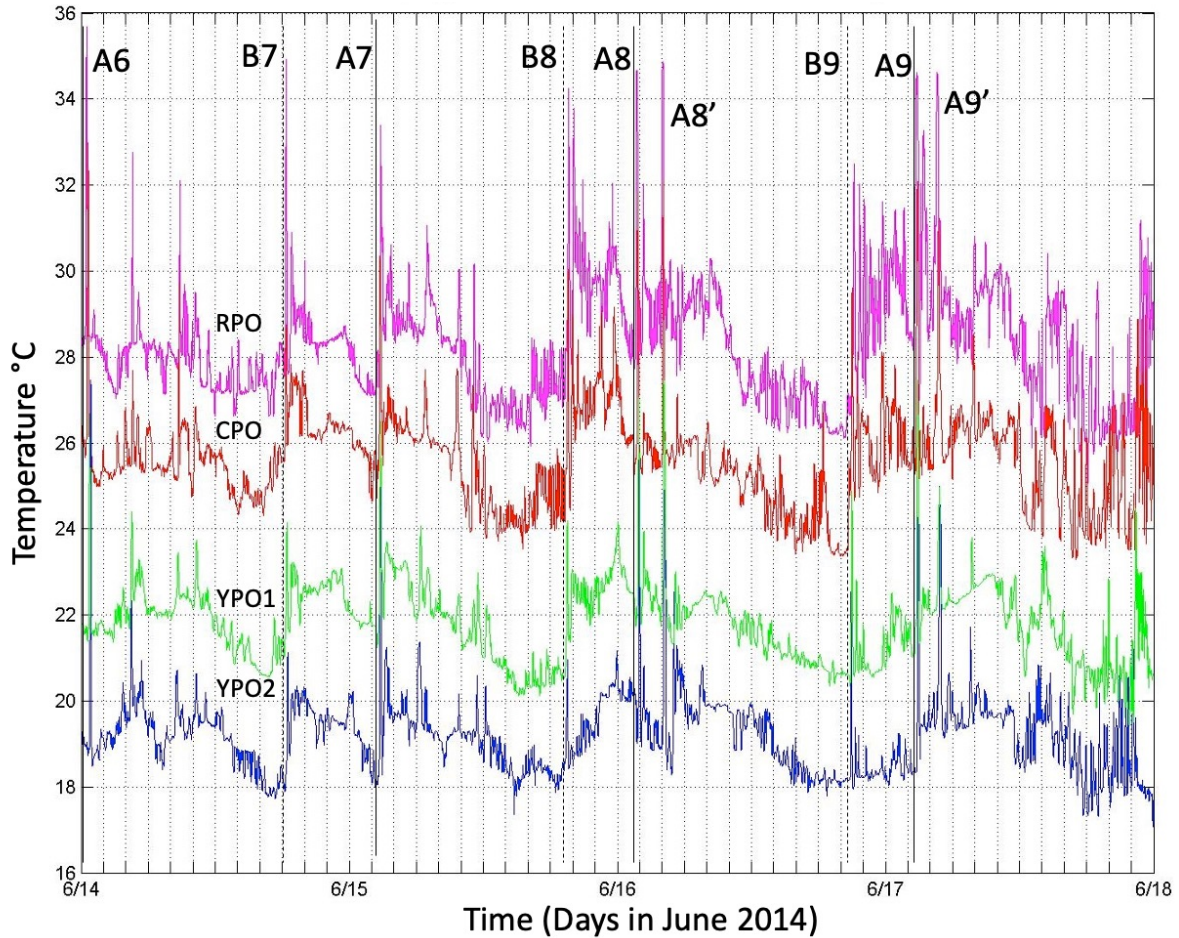
396

397 off-axis towards the northeast [Chang et al., 2006]. The Sand Dunes site is near the
 398 northeastern extremity of the wave crests as viewed in the imagery: a bit farther to
 399 the northeast the waves vanished. A practical ramification of this is that the
 400 undersea sand dunes were located in a region where the forcing due to encroaching
 401 NLIWs was not maximal. Other factors such as the bottom slope and sediment
 402 supply must also play an important role in determining the dune formation location.

403

404 The double A-wave phenomenon mentioned earlier (Figure 4) was again evident in
 405 Figure 7. These waves differed from the smaller waves trailing A5 and A6 in that
 406 they were already well-developed by the time they arrived at YPO2. As in Figure 6,
 407 many waves which were solitary at YPO2 formed packets as they crossed the array.
 408 Waves B9, A9, and A9' can be clearly seen in the satellite ocean color imagery
 409 (Figure 9). The timing of the imagery at 0310 was conveniently just as wave A9 was

410



411
412
413

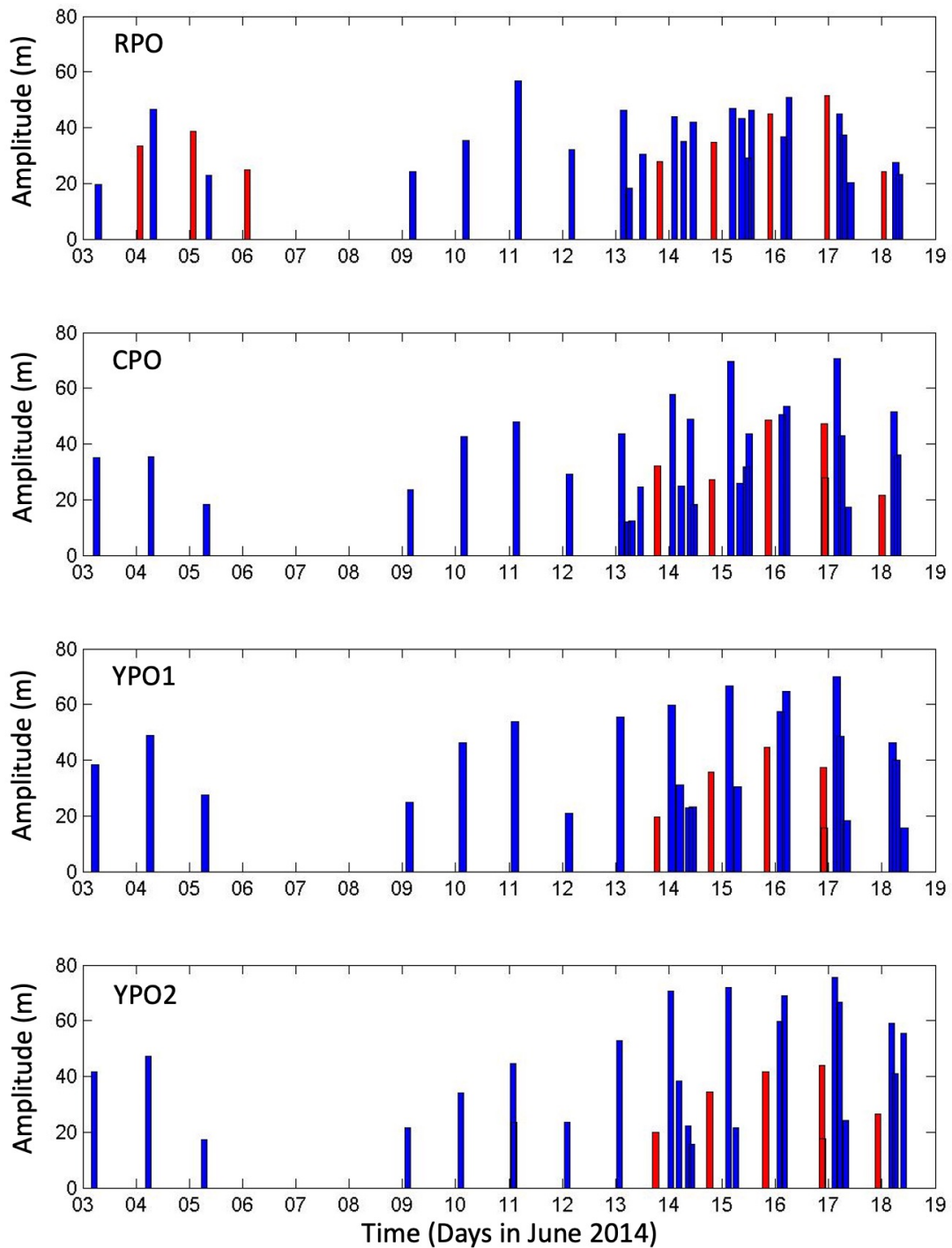
414 *Figure 7. As in Figure 6 except for June 14-18.*

415
416
417
418

416 impacting mooring YPO2. The B-wave packets and solitary nature of A9 and A9' are
417 easily seen in the image.

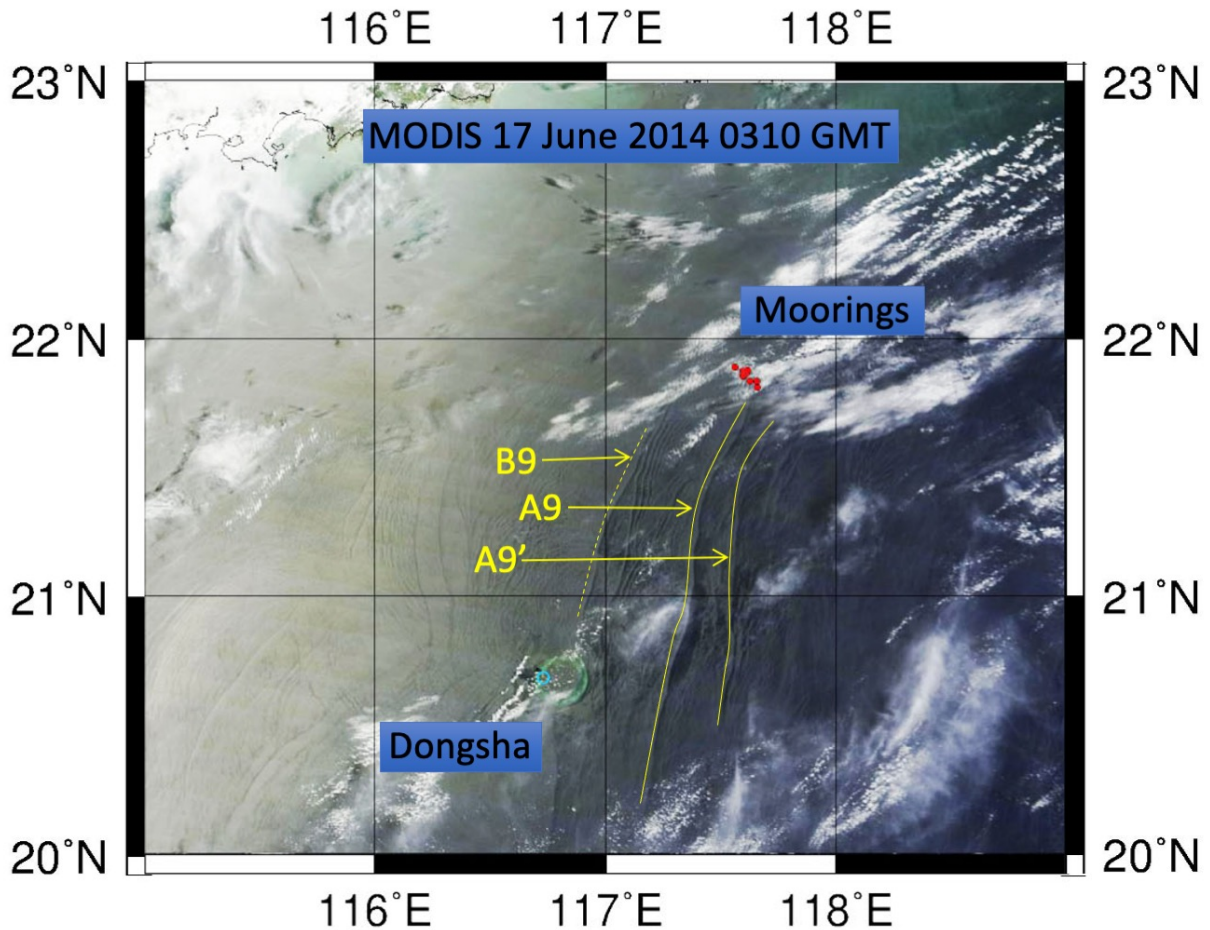
419
420
421
422
423
424
425
426
427
428
429
430

419 Two examples of velocity and temperature across the slope are shown to illustrate
420 the difference between weakly and strongly forced waves. Mooring YPO1 is not
421 shown since it was very similar to mooring YPO2 (Figure 10). The weaker case
422 begins at YPO2 on June 3-4 (Figure 10, column 1) which shows a clear a-wave near
423 0530 but no b-wave. Wave a2 was observed towards the rear of the
424 northwestward-propagating internal tide (blue near the surface). The a-wave was
425 traveling NW near the surface and in the opposite direction in the lower water
426 column, with a nodal point near 100 m. While not obvious in temperature, the
427 velocity plots show a weak second wave about 20 min behind the lead wave forming
428 a 2-wave packet. By mooring CPO (column 2), located 7.3 km away, the leading edge
429 of the internal tide had steepened to form a sharp front in both velocity and
430 temperature near midnight on June 3. There was strong convergence in the upper



431
 432
 433
 434
 435
 436
 437

Figure 8. Bar graph of wave amplitudes across the slope. The amplitudes were calculated as deviations of the 20 °C isotherm from its mean position. The a-waves are indicated by blue bars and the b-waves by the red.

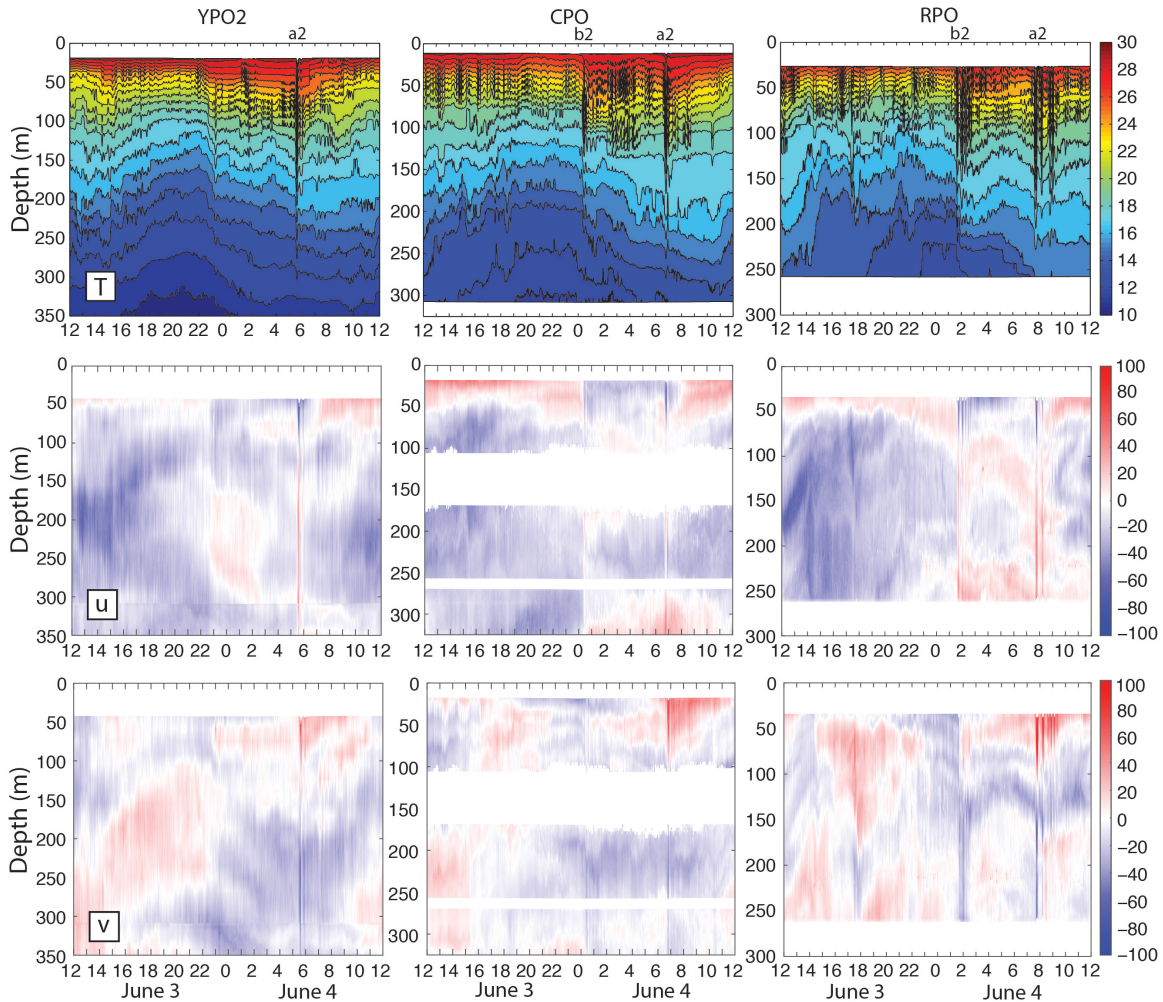


438
439

440 *Figure 9. A sea surface ocean color image obtained at 0310 on June 17, 2014 from the*
 441 *Moderate Resolution Imaging Spectroradiometer (MODIS). The Sand Dunes moorings*
 442 *are indicated by the red dots. The site of the former ASIAEX and WISE/VANS mooring*
 443 *S7 is indicated by the yellow triangle. The surface signatures of NLIWs B9, A9, and*
 444 *A9' are indicated by the yellow arrows. Wave A9 was impinging upon mooring YPO2 at*
 445 *this moment, as seen in Figure 7.*

446

447 50 m with eastward flow (red shades) ahead of the front and westward flow (blue
 448 shades) behind it. A solitary b-wave appeared on this convergent front which was
 449 absent at YPO2. Wave a2 at CPO looked similar to YPO2, perhaps slightly stronger.
 450 By mooring RPO, 5.7 km and 80 m farther up the slope (column 3), the b-wave
 451 increased in amplitude and formed a 2-wave packet, and the leading a-wave
 452 spawned a 4-wave packet. These waves were particularly clear in the v-component
 453 since the waves refracted towards the north as they propagated up the slope (Figure
 454 1). The nodal point remained near 100 m for all the leading waves. Note that the
 455 background internal tide (most easily seen in the deep water) was diurnal at
 456 moorings YPO2 and CPO but became more semidiurnal at RPO. This indicates the
 457 presence of a locally generated tide at RPO where the bottom slope was steeper than
 458 at the other moorings farther offshore. In fact, the bottom slope at YPO2-CPO



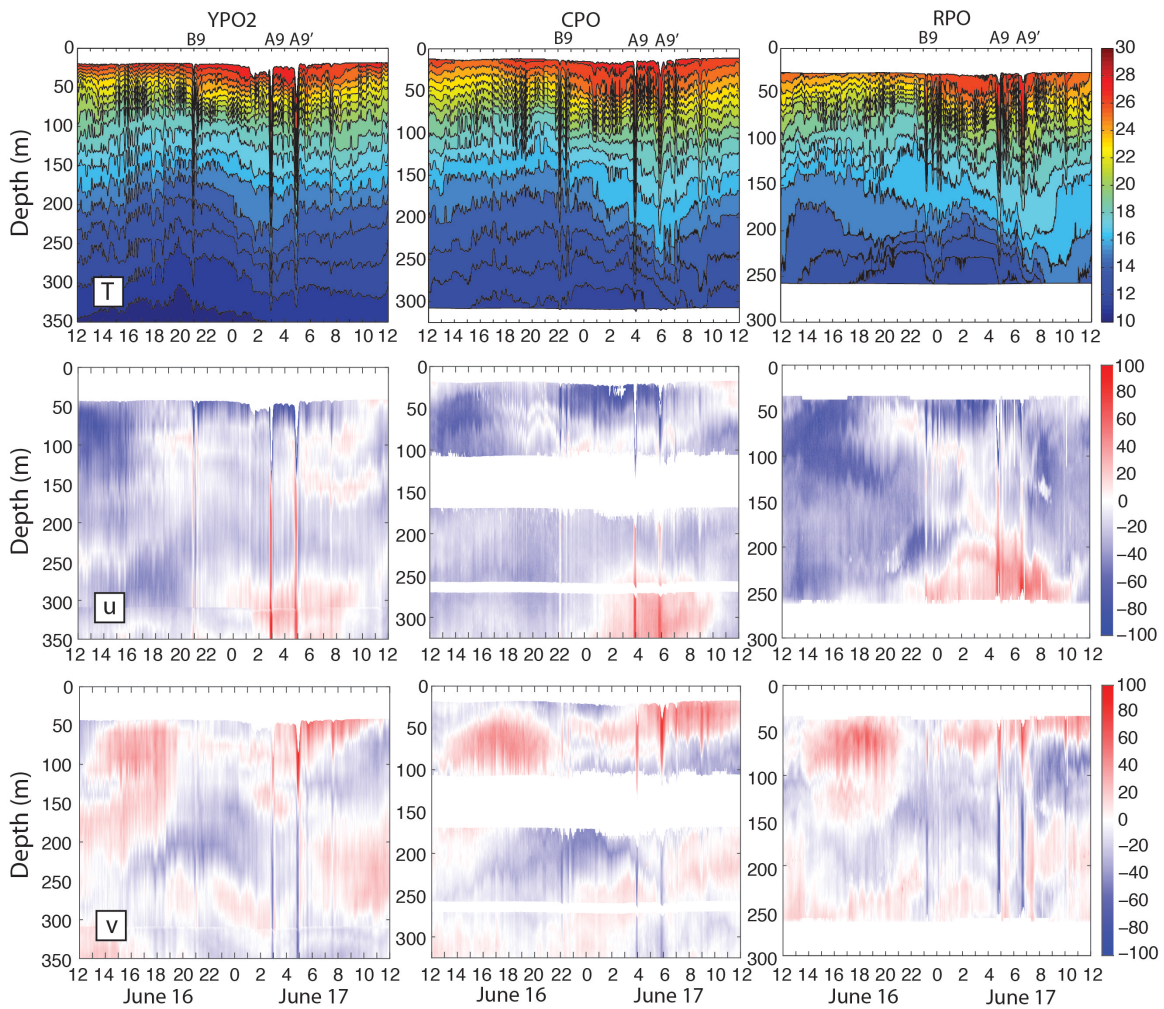
459
 460
 461
 462
 463
 464
 465
 466
 467
 468

Figure 10. Temperature (top), u -component of velocity (middle) and v -component of velocity (bottom) from 3-4 June 2014 from moorings YPO2 (left), CPO (center), and RPO (right). The wave propagation time between moorings was 67 min from YPO2 to CPO, and 56 min from CPO to RPO. Positive (u , v) represents (east, north) respectively. White space at mooring CPO indicates regions not sampled by the three ADCPs. These data were obtained during a period of moderate and declining tidal forcing, see Figures 3 and 5 for context.

469 (Figures 1, 2 right of the dotted white line) was critical to the diurnal tide while the
 470 slope at RPO (left of the dotted white line) was critical to the semidiurnal tide. The
 471 interaction of the tidal currents with the bottom is maximal where the slope of the
 472 tidal beams parallels the bottom and this likely contributes to the different nature of
 473 the sand dunes offshore vs. onshore of the dotted white line (Figure 2). At all
 474 moorings, there was only one westward surface internal tide per day. The b -waves
 475 all emerged at the leading edge of this westward tide, while the a -waves emerged
 476 towards the rear, and this clear velocity signature represents another way to
 477 distinguish the two types of waves. The two wave arrivals were separated by 6:20

478 on this day. The strongest bottom velocities were down-slope (southeast) and were
 479 greater in the NLIW than in the internal tide.
 480

481 The strong example (Figure 11) shows that unlike the previous example, both the B-
 482 wave packet and the A-wave packet had already formed by mooring YPO2 on June
 483 16-17. (Remember there is no dynamical significance to upper vs. lower case a, b:
 484 the lettering is chosen to remain consistent with the nomenclature established in
 485 the earlier figures and refers to the first and second cluster.) The waves were
 486 traveling in the same direction as the June 3-4 waves, but had a deeper nodal point
 487 located near 120-130 m. The A-wave in this case was a double A-wave mentioned
 488 earlier. These resembled individual waves rather than a packet in the usual sense.
 489 The two waves A9 and A9' were about the same amplitude: on this day the first
 490 wave (A9) was slightly larger, but the opposite was true the day before (not shown).
 491 The A9' wave was slightly wider than the A9 wave. This may be due to constructive
 492



493
 494
 495
 496
 497

Figure 11. As in Figure 10, except for June 16-17, 2014. These data were obtained during a period of strong tidal forcing, see Figures 3 and 7 for context.

498 interference with the tail of wave A9 which was just two hours ahead of it. Wave B9
499 formed a 2-wave packet at CPO (column 2) and a 3-wave packet at RPO (column 3).
500 Wave A9 formed a 2-wave packet between moorings CPO and RPO. As before, the u-
501 component shows the B-wave was coming off the leading edge of the westward
502 surface tide (eastward bottom tide). The A9 wave grew out of the middle of the tide
503 and the A9' wave emerged from the trailing edge of the same westward internal
504 tide. The surface westward velocities exceeded 97 cm s^{-1} , 162 cm s^{-1} , and 153 cm s^{-1}
505 at YPO2, CPO, and RPO respectively. The eastward bottom velocities exceeded 20
506 cm s^{-1} , 85 cm s^{-1} , and 80 cm s^{-1} respectively. The smaller lower layer velocities
507 below the nodal point were consistent with a thicker lower layer and with theory
508 [Lamb and Warn-Varnas, 2015]. The strongest bottom velocities outside the waves
509 were about half the wave velocities. Clearly the strongest bottom velocities
510 observed over the upper continental slope were generated by the passing NLIWs,
511 although these high velocities were very brief compared to the internal tide.
512 Referring once again to Figure 8, the B-wave (just before midnight on June 16)
513 started at YPO2 with just over 40 m amplitude and grew shoreward across the shelf.
514 In contrast, the much larger A-waves just after midnight on the 17th started out
515 with 70 – 75 m amplitude at YPO2 and lost amplitude across the shelf. This is
516 consistent with the earlier discussion surrounding Figure 10.

517

518 Many ordinary internal waves can be seen in Figure 11 in between the nonlinear
519 waves. These waves were likely generated by tropical cyclone Hagabus which
520 passed over the array on June 14-15 with winds exceeding 25 m s^{-1} .

521

522 On June 16 a packet of convex mode-2 waves appeared from 1500-2100 centered
523 near 60 m and extending from 50 to 100 m depth (Figure 11, bottom row). These
524 waves strengthened upslope from YPO2 to RPO and trailed the double-A waves
525 from the day before (not shown). There looked to be about 6 waves in the mode-2
526 packet at mooring RPO. All three of the double-A waves on 16, 17, and 18 June had
527 this feature associated with them. The observation is consistent with [Yang et al.,
528 2009, 2010] who observed mode-2 waves trailing mode-1 waves in the ASIAEX
529 region nearby and attributed this to the adjustment of shoaling mode-1 waves.
530 These observed wave transformations are now discussed further below in light of
531 the theory for shoaling solitary waves.

532

533 **4 Discussion**

534

535 *4.1 Theoretical Framework*

536 In this section, the observed NLIW characteristics are compared with laboratory and
537 numerical studies to determine what kind of changes might be expected as the waves
538 shoal over the sand dunes region. The possibilities include adiabatic shoaling, dispersion,
539 breaking, and conversion to waves of elevation. The latter may be easily ruled out for
540 this study since this only happens when the nonlinear coefficient α from the KdV
541 equation changes sign, which typically takes place between 100 – 120 m depth over the
542 Chinese continental shelf [Hsu and Liu, 2000; Orr and Mignerey, 2003; Liu et al., 2004].

543 Even accounting for some temporal variability due to the local internal tides, this “critical
544 point” where the upper- and lower-layer depths were equal was always well inshore of
545 the sand dunes region.

546 The wave progression WNW from deeper to shallower water may be conveniently
547 framed in terms of the two regions demarcated by the dotted white line in Figure 2.
548 Moorings YPO1, YPO2, CPO were all located in the region where the mean bottom slope
549 was $.006 = 0.6\% = 0.3$. Mooring RPO was in the region where the bottom slope was 0.03
550 $= 3\% = 1.7$ degrees. The bottom slope is considered gentle when it is less than $0.03 =$
551 1.7° [Grimshaw et al., 2004; Vlasenko et al., 2005; Lamb and Warn-Varnas, 2015;
552 Rivera-Rosario et al., 2020]. Dynamically speaking then the mean bottom slopes in the
553 sand dunes region ranged from weak to practically flat. Under these conditions, the
554 response of shoaling NLIWs depends primarily on three factors: the bottom depth, wave
555 amplitude, and thermocline depth [Small, 2001; Vlasenko and Hutter, 2002; Lamb, 2002;
556 Vlasenko and Stashchuk, 2007; Grimshaw et al., 2014; Lamb and Warn-Varnas, 2015;
557 Rivera-Rosario et al., 2020]. Waves can potentially break when wave orbital velocity
558 $u_{max} >$ the propagation speed c [Lien et al., 2014; Rivera-Rosario et al., 2020; Chang et
559 al., 2021b] and

$$560 \quad a_m > (H_b - H_m)0.4 \quad (1)$$

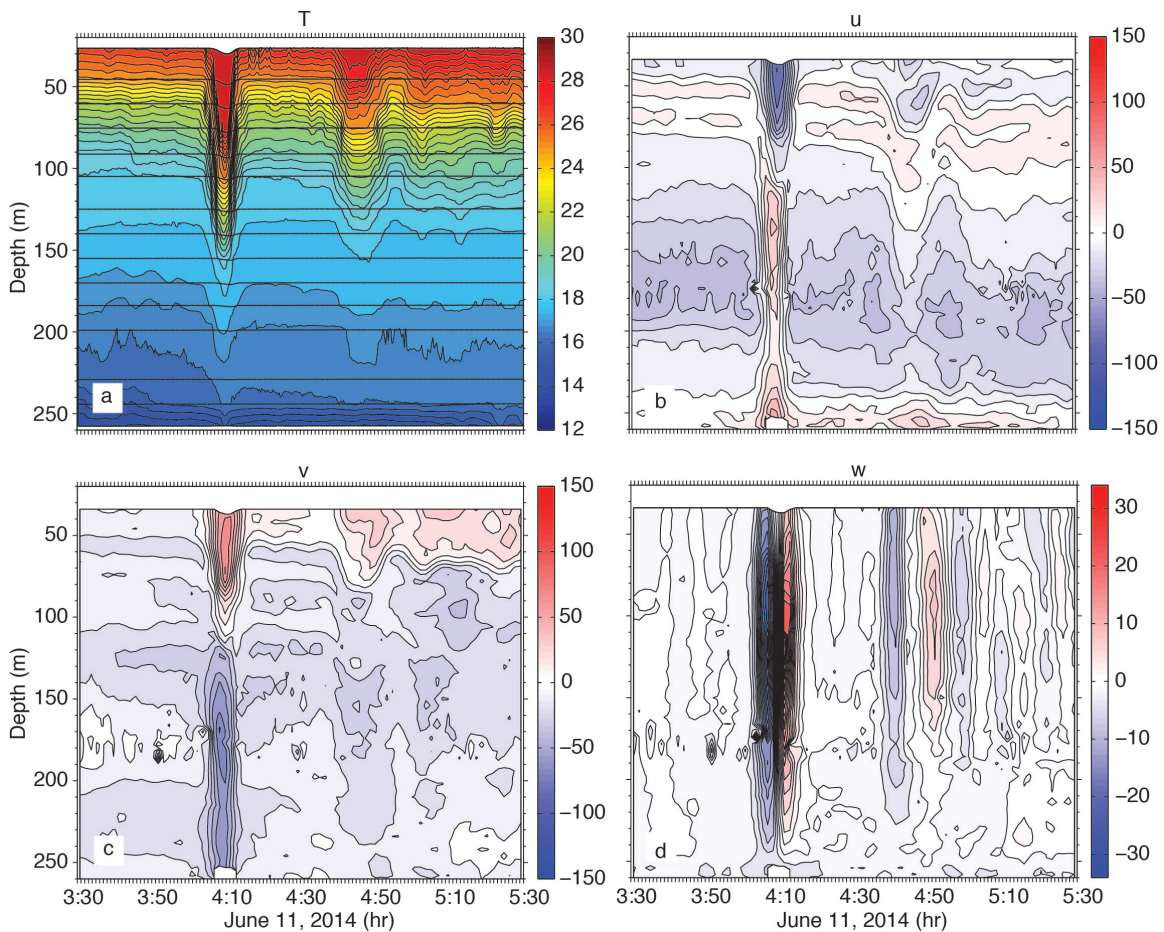
561
562 where a_m is the maximum possible wave amplitude, H_b is the bottom depth, and H_m is the
563 upper layer thickness, here approximated by the thermocline depth [Helfrich and
564 Melville, 1986; Helfrich, 1992; Vlasenko and Hutter, 2002]. This expression can be used
565 to evaluate the isobath where a wave of given amplitude will break, or alternatively, to
566 determine the wave amplitude necessary for wave breaking at a given isobath. For the
567 Sand Dunes data set, these criteria were examined for moorings CPO in region 1 and
568 RPO in region 2. The depth of the 23°C isotherm was used to estimate the thermocline
569 depth at both moorings. The undisturbed isotherm depth, determined by time-averaging
570 the low-pass filtered data, was similar at both moorings, 60 m at CPO and 57 m at RPO.
571 Substituting these values in (1) shows that a wave amplitude of 112 m would be required
572 at CPO for wave breaking to occur. Moving on to RPO, the required amplitude for wave
573 breaking there would be about 84 m. Comparing with the observed wave amplitudes at
574 CPO and RPO (Figure 8), all the observed wave amplitudes were less than the above
575 criteria, and no wave breaking events are expected in this array. Some combination of
576 adiabatic shoaling and packet formation via wave dispersion is more likely instead.

577
578 Using this guidance, the temperature and velocity structure at site RPO is studied in
579 greater detail for three examples: a statistically common a-wave (Figure 12), a very
580 large a-wave (Figure 13) and a b-wave (Figure 14). For wave A3 on June 11 (Figure
581 12), which typifies A-waves between June 3-13, the wave was symmetric in both
582 velocity and temperature with no sign of back-side steepening. The wave amplitude
583 was 57 m, and the maximum orbital velocity was 1.04 m s^{-1} and was located near
584 the surface. This was much less than the local phase speed of 1.60 m s^{-1} . The
585 opposing lower layer velocity was order 0.75 m s^{-1} commensurate with the thicker
586 lower layer. Such bottom velocities were commonly observed and are easily enough

587 to produce both bedload and suspended sediment transport among the dunes
588 [Reeder et al., 2011]. The w-profile was nearly symmetric at $\pm 0.25 \text{ m s}^{-1}$, downward
589 ahead of the wave and upward behind it, with the maxima located near mid-depth.
590 One or possibly two trailing waves were observed: the first was centered near 4:48
591 and had vertical velocities of $\pm 0.8 \text{ m s}^{-1}$ while the second was near 5:00 with
592 vertical velocities of just a few cm s^{-1} . A fourth wave-like feature was observed in
593 the temperature plot near 5:20 but it cannot be discerned in the velocity structure.
594 To summarize, wave A3 consisted of a primary wave and 2-3 trailing waves about
595 30 min behind. The wave was symmetric in velocity and temperature with no sign
596 of breaking or trapped core formation.

597
598 The largest wave observed was wave A9 on June 17. This wave showed several
599 characteristics of breaking or near-breaking waves (Figure 13). The back side of the
600 wave was steeper than the leading side, and the jagged temperature contours in the
601 wave core were indicative of breaking and/or mixing. A “pedestal” was starting to
602 form behind the wave as described by [Lamb and Warn-Varnas, 2015]. Several
603 more smaller depression waves were emerging from the “pedestal.” The velocity
604 contours were likewise asymmetric and showed a subsurface maximum near 60-70
605 m which was about 0.20 m s^{-1} greater than the surface. This is typical of waves with
606 trapped cores [Lien et al, 2012, 2014; Lamb and Warn-Varnas, 2015]. The
607 maximum near-surface velocity was 1.55 m s^{-1} , which was close to the local phase
608 speed (1.60 m s^{-1}). It is possible that the surface velocities above 20 m depth were
609 slightly larger but were not observed. At site CPO, this same wave had a maximum
610 velocity of 1.80 m s^{-1} , also very close to the local phase speed. The vertical velocities
611 were actually smaller than wave A3, at -12 and $+20 \text{ cm s}^{-1}$ with at least two and
612 possibly more of the trailing depression waves visible as down/up pairs. To
613 summarize, this wave appears to be about to break or just starting to break,
614 however, this wave was the exception rather than the rule: only one such wave was
615 observed. It is possible that the trailing double-A waves A8' and A9' might also meet
616 these criteria, however their form was distorted by interference from the trailing
617 packet of the leading A8 and A9 waves two hours earlier, making their
618 characteristics difficult to discern. The South China Sea NLIW amplitudes in June
619 are near their maximum values observed in July and August [Chang et al., 2021a]. It
620 is thus unlikely that breaking waves are ever prevalent in the sand dunes region.
621 This situation contrasts with a similar depth range farther southwest, where larger
622 waves were already actively breaking at the 300 m isobath [Chang et al., 2021b].

623
624 It is worth noting that subsurface velocity maximum in the wave may be caused by
625 phenomena other than wave breaking. Tropical cyclone Hagabus passed over the
626 array on June 14-15 and forced strong near-surface currents which opposed the
627 wave velocities. This was especially obvious on June 15 (not shown) when
628 westward currents at 80 m depth in wave A7 exceeded the surface currents by over
629 0.80 m s^{-1} at RPO and by over 1.00 m s^{-1} at CPO. This likely explains why wave A7
630 arrived 2 hours late with respect to waves A6 and A8 (Figure 4). The storm also left
631 behind a surface mixed layer 40 m deep which lingered to the end of the record.
632 This means all the largest waves forced near spring tide propagated into a region



634

635

636

637 *Figure 12. a) temperature, b) u-component of velocity (positive east), c) v-component*
 638 *of velocity (positive north), and vertical velocity (positive up) for wave A3 on June 11,*
 639 *2014. This rank-ordered packet with a symmetrical leading wave typifies most of the*
 640 *type-a waves observed during the experiment.*

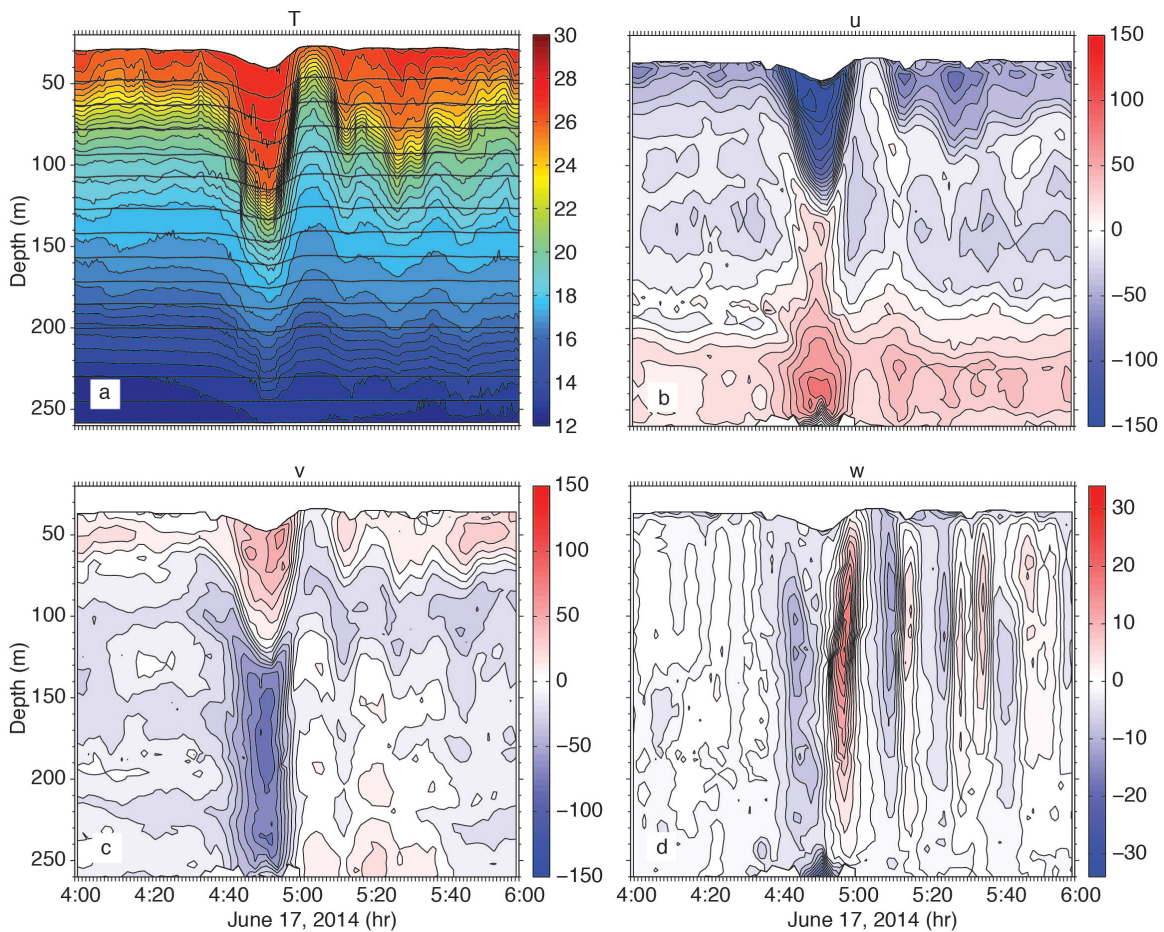
641

642 with an unusually deep surface mixed layer. The effect of this is to severely limit
 643 wave breaking [Lamb, 2002]. In fact, the scenario described above in the results
 644 section rather closely resembles the model results of [Lamb, 2002] when a surface
 645 mixed layer was added (their Figure 10). The shoaling solitary wave in the model
 646 produced a second trailing solitary wave, followed by the dispersive tail of mode-1
 647 depression waves, followed by a packet of mode-2 waves. The observations
 648 reported here closely resembled this pattern not only on June 16-18, but also on
 649 June 3-5 trailing waves a1 and a2.

650

651 We conclude that most of the packets that formed as the waves traveled up the
 652 slope from YPO2 to RPO were formed by dispersion rather than wave breaking.
 653 Rotational effects seem locally unimportant, given that the packets formed in just
 654 two hours while the local inertial period was 32 hours. Rotation may have played a

655



656

657

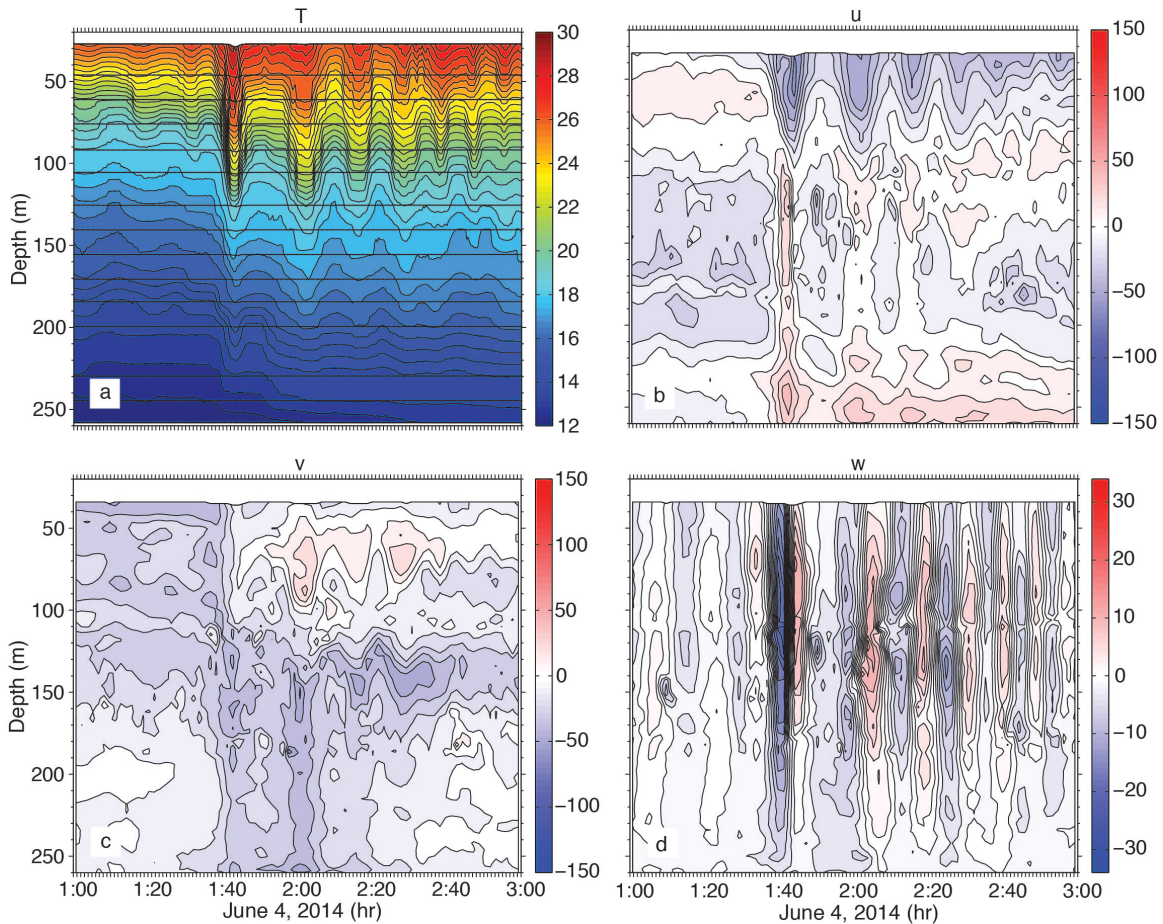
658

659 *Figure 13. As in Figure 12, but for wave A9 on June 17, 2014. The steepening back side*
 660 *and subsurface velocity maximum suggest breaking or imminent breaking.*

661

662 role farther offshore, establishing the initial perturbations (inertial gravity waves)
 663 that then grow and become a trailing packet as the waves shoal [Grimshaw et al.,
 664 2014]. This effect could not be investigated without observations in deep water.
 665 Trailing undular bores of the sort modeled by [Grimshaw et al., 2014] by including
 666 rotation were not observed, but are likely not observable since in the real ocean, the
 667 waves arrive periodically and the trailing undular bores would be destroyed by each
 668 subsequent arriving NLIW before they have a chance to develop. It is most likely
 669 then an imbalance between nonlinearity and dispersion that causes the new trailing
 670 waves to form [Vlasenko and Hutter, 2002; Lamb and Warn-Varnas, 2015]. The
 671 large lead ISW in the Sand Dunes array never split in two, but rather slowly
 672 decreased in amplitude as energy was transferred to the dispersive tail. Phenomena
 673 such as wave splitting and breaking likely took place inshore of the sand dunes
 674 array in the vicinity of the 150 m isobath, as was observed previously at the ASIAEX
 675 site nearby.

676



677
 678 *Figure 14. As in Figure 12, except for wave b2 on June 4, 2014. This example typifies*
 679 *waves formed locally by breaking of the tidal front between moorings YPO and RPO.*
 680

681 The situation for the locally formed b-waves (b2-b4) was completely different.
 682 These waves were non-existent at YPO2 but formed well-defined, evenly spaced
 683 packets by the time they reached RPO (Figure 14). For wave b2 on June 4, six waves
 684 can be clearly seen in T and w, with most all the horizontal velocity in u, that is these
 685 waves were traveling westward. The amplitude of the lead wave was about 40 m,
 686 the near surface velocity 60 cm s^{-1} westward, and near-bottom velocity 40 cm s^{-1}
 687 eastward. The waves were formed all at once by the collision and breaking of the
 688 westward internal tide with the off slope propagating eastward tide. This is a
 689 different mechanism than that described for shoaling ISWs in the literature.

690
 691 *4.2 Energy and energy flux*
 692

693 The data set provides an opportunity to observe how the horizontal kinetic (HKE)
 694 and available potential (APE) energy in the high-frequency nonlinear internal waves
 695 changes as the waves propagate up a gentle slope. In turn, the energy pathways
 696 provide some insight to the dynamics underlying the wave transformation process.

697 The theoretical expectation for linear and small-amplitude nonlinear internal waves
698 is that the energy will be equipartitioned for freely propagating long waves away
699 from boundaries. This is not the case however for finite amplitude nonlinear,
700 nonhydrostatic internal solitary waves whose KE typically exceeds the PE by a
701 factor of 1.3. This result was found theoretically via exact solutions to the fully
702 nonlinear equations of motion [Turkington et al., 1991] and has also been noted
703 observationally [Klymak et al., 2006; Moum et al., 2007]. Thus, the KE is expected to
704 slightly exceed the PE for the waves arriving at mooring YPO2. For shoaling NLIW
705 however, the flux of PE theoretically exceeds the flux of KE which causes the PE to
706 exceed the KE in shallower water [Lamb, 2002; Lamb and Nguyen, 2009]. This is
707 because the flux of PE remains nearly constant while the KE flux decreases as the
708 upper- and lower-layer thicknesses become more equal. Shoaling waves observed
709 in the Massachusetts Bay displayed this property [Scotti et al., 2006]. Thus, a shift
710 from greater KE to greater PE might be expected as the waves shoal from YPO2 to
711 RPO, although it depends on the details of the wave amplitude, stratification, bottom
712 slope, etc.

713

714 To compute the energies and energy fluxes from moorings, time series of density
715 and velocity which are uniform in space and time are required. Moorings RPO and
716 CPO had good coverage of temperature and salinity in the vertical (Appendix A)
717 however moorings YPO1 and YPO2 sampled temperature only. Two methods to
718 compute the density at YPO1 and YPO2 were explored. The first used a constant
719 salinity (34.42, the vertical average from a nearby CTD cast) paired with the
720 observed temperature at each sensor to compute density. This method assumes
721 that most of the density variability comes from the temperature fluctuations rather
722 than salinity. The second method used the salinity profiles from all the CTD casts
723 taken during the cruise to compute a mean T/S curve, which was then used as a
724 look-up table to determine the salinity to use with each observed temperature. The
725 CTD casts were all within 12 km of each other and were thus treated as a time
726 series. The profiles fell into two groups, namely before tropical storm Hagabus
727 passed by on June 14, with little-to-no surface mixed layer, and after the storm when
728 the mixed layer was about 40-50 m deep. Thus, two mean T/S curves were actually
729 used, one from before the storm and one after. The benchmark for these methods
730 was to compare the density calculated using the T/S curves with the actual density
731 calculated using the observed salinity on moorings RPO and CPO. The APE
732 computed using the mean T/S curve was found to agree much better with the
733 observations than the APE computed using a constant value for the salinity. Both
734 techniques were slight underestimates of the true APE, but the T/S method much
735 less so than the constant method. For this reason, the mean T/S curves were used
736 to compute the density time series, and thus APE for moorings YPO1 and YPO2.

737

738 The observed time series also had velocity gaps of varying severity in the water
739 column due to the range limitations of the ADCPs. Mooring CPO had a mid-depth
740 gap spanning roughly 110-170m and a second smaller gap from 255-265m (see
741 Figures 10 and 11). These gaps were filled using the least squares fit normal mode
742 techniques described in [Nash et al., 2005]. Theoretically as many as seven modes

743 (number of instruments in the vertical – 1) were possible, but the most stable
 744 results were achieved with just three modes. No attempt was made to fill in the
 745 upper 20 m of the water column where both velocity and temperature were
 746 unsampled by the moorings.

747
 748 Once clean time series were available to operate on, the energies and energy fluxes
 749 were computed from the data via established techniques [Nash *et al.*, 2005, 2006;
 750 Lee *et al.*, 2006]. The baroclinic velocity and pressure fluctuations induced by the
 751 waves were first computed as

$$752 \quad \bar{u}'(z,t) = \bar{u}(z,t) - \bar{u}(z) - \frac{1}{H} \int_{-H}^0 [\bar{u}(z,t) - \bar{u}(z)] dz \quad (1)$$

754
 755 and
 756

$$757 \quad p'(z,t) = g \int_z^0 \rho'(\xi,t) d\xi - \frac{g}{H} \int_{-H}^0 \int_z^0 \rho'(\xi,t) d\xi dz \quad (2)$$

758
 759 where

$$760 \quad \rho'(z,t) = \rho(z,t) - \bar{\rho}(z) \quad (3)$$

762
 763 is the density anomaly with respect to the time-mean density profile. In equations
 764 (1) and (2), the last term satisfies the baroclinicity requirement that the primed
 765 quantities integrate to zero over the entire water column [Kunze, *et al.*, 2002]. Over
 766 bars indicate temporal means. The HKE and APE can then be computed as

$$767 \quad HKE = \rho_0 (u'^2 + v'^2) / 2 \quad (4)$$

$$768 \quad APE = \frac{1}{2} \frac{g^2 \rho'^2}{\rho_0 N^2} \quad (5)$$

770
 771 where ρ_0 is the mean density, g is the acceleration of gravity and N^2 is the buoyancy
 772 frequency.

773
 774 The energy flux due to highly nonlinear internal waves is given by

$$775 \quad \vec{F}_E = \bar{u}'(p' + HKE + APE) \quad (6)$$

777
 778 where the first term on the right is the pressure work and the second and third
 779 terms represent the advection of horizontal kinetic and available potential energy
 780 density [Nash *et al.*, 2012]. For the small amplitude, linear, hydrostatic case the flux
 781 equation is often approximated as the first term only

782

$$783 \quad \vec{F}_E = \vec{u}'p' \quad (7)$$

784

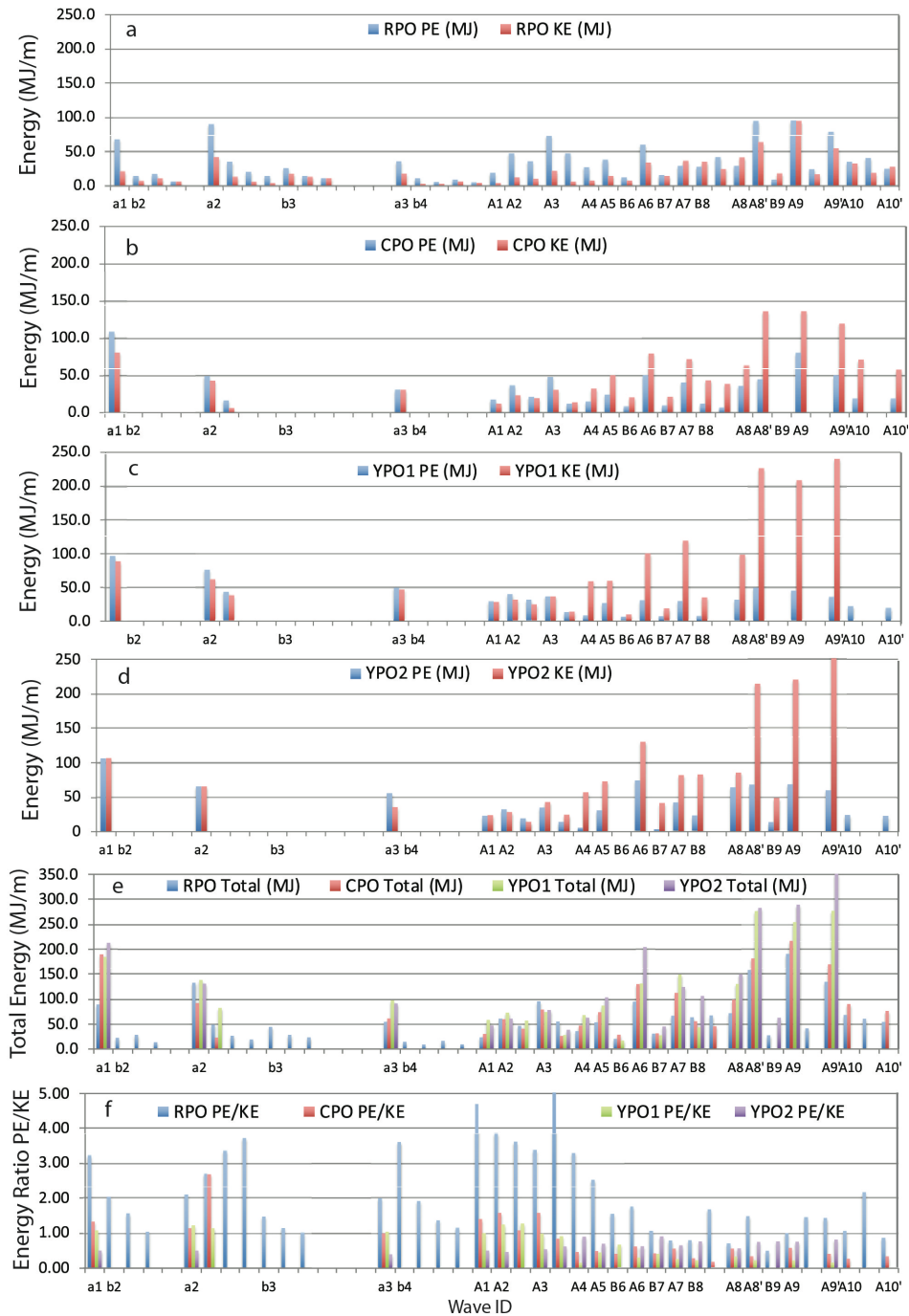
785 but since it is not obvious that this approximation is valid for the strongly nonlinear
786 shoaling waves observed in the sand dunes region, all three terms of the flux
787 equation were computed.

788

789 The resulting changes in the wave energy distribution across the slope depended on
790 the wave amplitude (Figure 15). For waves up to and including A3 on June 11, the
791 APE exceeded HKE offshore and continued to increase up the slope. This is
792 interpreted to mean the waves were still growing and had not yet reached
793 maximum amplitude. Smaller waves can penetrate farther upslope adiabatically
794 than larger waves. Wave A4 was anomalously small for which no obvious
795 explanation has been found. Perhaps the wave was obliterated by the leading edge
796 of tropical storm Hagabus. Starting with wave A5 on June 13, as the remote
797 barotropic tidal forcing continued to increase, the HKE exceeded APE at YPO2 by a
798 factor averaging 1.7 and increased to its maximum value at mooring YPO1. This
799 ratio is even larger than the theoretical expectation of 1.3 [Turkington 1991; Lamb
800 and Nguyen, 2009] and indicates highly nonlinear waves with large amplitudes.
801 Between CPO and RPO, there was a dramatic change when the APE increased and
802 the HKE sharply decreased, resulting in greater APE than HKE at mooring RPO
803 (Figure 15a). The energy ratio at RPO (Figure 15f) was commonly three to four but
804 suddenly decreased sharply with the arrival of wave A6 on June 14 and remained
805 near one for the remainder of the time series. This is attributed to the increased
806 surface mixed layer depth as the tropical storm went by which wiped out the upper
807 ocean stratification and reduced the APE. The total energies (Figure 15e) integrated
808 both vertically and over a wavelength, followed an envelope consistent with the
809 remote tidal forcing and maxed out at around 250 MJ m⁻¹. This was less than half
810 the energy (550 MJ m⁻¹) previously reported over the Dongsha Plateau [Lien et al.,
811 2014] where the maximum observed wave amplitudes exceeded 150 m vs. 80 m
812 here. The total energy appears approximately conserved across the slope for many
813 of the waves as indicated by color bars of approximately equal length (Figure 15e).
814 The losses in HKE were compensated for by the increases in APE, in reasonable
815 agreement with theory and numerical simulations [Lamb and Nguyen, 2009; Lamb
816 and Warn-Varnas, 2015]. For the larger waves however, such as a1, A6, A8', A9, and
817 A9' the total energy decreased upslope (Figure 15e). The HKE was lost much faster
818 than the APE was gained. This is attributed to strong dissipation over the rough
819 bottom in the dune field [Helfrich et al., 2022].

820

821 In the simplest sense the energy flux is just the energy times the group velocity (or
822 phase velocity for non-dispersive waves). Since the phase velocity varied from 1.87
823 m s⁻¹ between YPO2 and YPO1 to 1.69 m s⁻¹ from CPO to RPO, the flux/energy ratio
824 is expected to vary little across the slope and the flux patterns should resemble that
825 of the total energies. This is indeed the case as seen by comparing the envelope of
826 the curves for the total flux (Figure 16b) and the total energy (Figure 15e). The



827
 828
 829
 830
 831
 832
 833

Figure 15. Energy transformations across the slope. The total HKE and APE, computed by integrating the wave energy both vertically and horizontally at moorings RPO, CPO, YPO1, and YPO2 are shown in panels a-d respectively. The total pseudo-energy (HKE + APE) at all four moorings is shown for each wave in panel e, and the APE/HKE ratio in panel f.

834 vertically integrated flux tends to decrease upslope primarily due to the decreasing
835 water depth. Of greater interest is the change in the various terms of equation (6).
836 The pressure work is indeed the largest term but not by much: The PW comprised
837 57%, 56%, 43%, and 52% of the total flux at YPO2, YPO1, CPO, and RPO
838 respectively. The large percentage still remaining was accounted for by the
839 advection of HKE and APE and shows that the waves were indeed strongly
840 nonlinear. The increase in APE with respect to HKE at mooring RPO versus CPO can
841 be accounted for by the change in the fluxes at those moorings (Figure 16a). From
842 CPO to RPO, the kinetic energy flux dropped by 50% (blue line to green line) while
843 the potential energy flux went up slightly (red line to purple line).

844

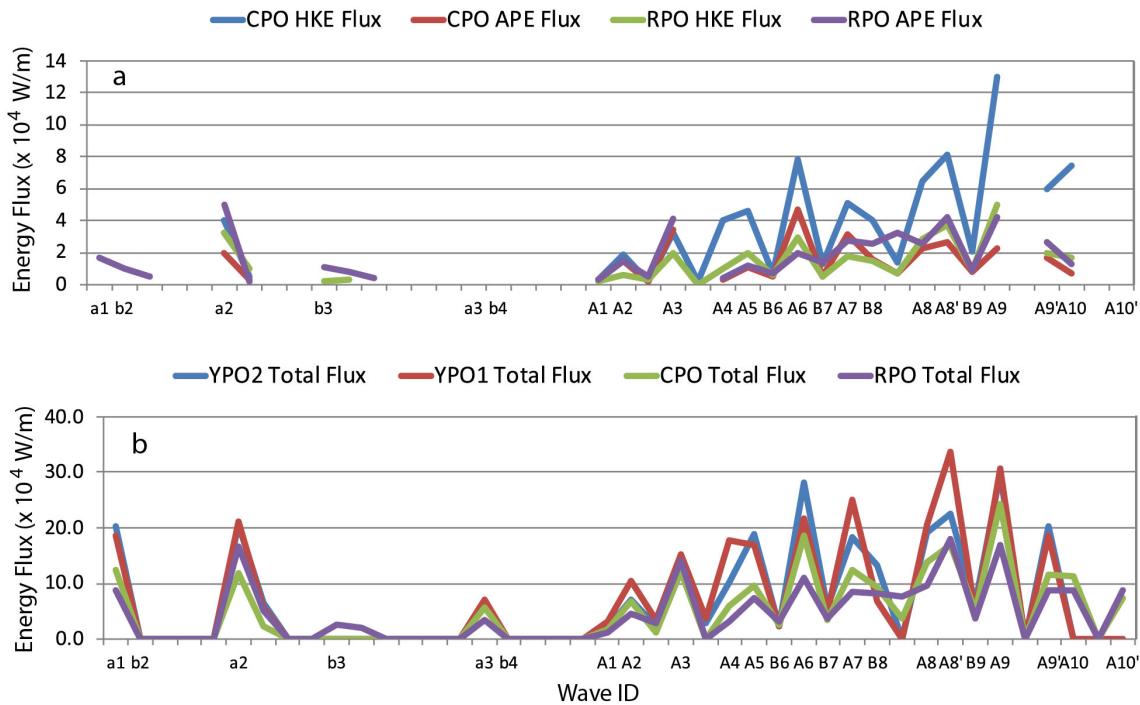
845 **5. Summary and conclusions**

846

847 An 18-day time series of high-resolution velocity and temperature data were
848 obtained at four closely spaced moorings spanning 386-266 m depth on the
849 continental slope 160 km northeast of Dongsha Island in the South China Sea. The
850 experiment was motivated by the need to understand ocean variability and how it
851 interacts with large (15 m) sand dunes on the sea floor. The dominant signal
852 observed consisted of sets of large amplitude nonlinear internal waves (NLIWs)
853 impinging on the continental slope from the southeast. These were in fact the very
854 same waves that impact the Dongsha Island region and have been reported by many
855 previous authors. The “sand dunes” waves however were about 50% smaller and
856 less energetic than the “Dongsha” waves, since the location was near the northern
857 extremity of the wave crests rather than near the main axis of the waves. The mean
858 bottom slope along the sand dunes mooring line was also gentler than farther
859 southwest. While the internal tides are no doubt important to the dune-building
860 process, this paper focuses entirely on the NLIW properties, most especially how the
861 waves were transformed as they shoaled up a very gradual bottom slope. New
862 information gleaned includes the packet formation process, further insights on the
863 difference between a-waves and b-waves, and the energy transformation processes
864 which took place during wave shoaling.

865

866 During the fortnight observed, the a-waves began arriving several days ahead of the
867 b-waves and traveled in a more northerly direction. Once they started arriving, the
868 b-wave always lead the a-wave by 6-8 hours. In any given pair, the a-wave was
869 generally larger, but b-waves generated near spring tide may be larger than a-waves
870 generated near neap. The a-waves generally arrived at the site as 2-3 wave packets,
871 but the b-waves may also form packets as they shoal. The wave generation location
872 and their positioning relative to each other and the internal tide determines the
873 wave classification. The b-waves were located near the head of the upslope internal
874 tide while the a-waves developed more towards the back. The wave arrival patterns
875 rigorously tracked the tidal structure in Luzon Strait, even to the point of shifting by
876 six hours when the strong beat/weak beat pattern reversed in the strait during neap
877 tide. The arrival patterns were consistent with earlier work showing that the a-
878 waves were generated in the southern portion of the Luzon Strait and the b-waves
879 in the north.



880
881

882 *Figure 16. The energy fluxes up the slope for each of the nonlinear internal waves*
 883 *identified in the sand dunes moored array data. a) The kinetic and potential energy*
 884 *flux for moorings CPO and RPO. b) The total energy flux for all four moorings. This is*
 885 *the sum of the kinetic, potential, and pressure work terms.*

886

887 A conundrum remains the arrival of two large a-waves with nearly equal amplitude
 888 separated by two hours during the period of maximal tidal forcing, spring tide plus
 889 or minus one day. Additional work is needed to understand the origin of these
 890 waves.

891

892 At least two packet-generating mechanisms were clearly observed. Most a-waves
 893 had already formed in the deep basin by the time they were incident upon the most
 894 offshore mooring, YPO2 at the 388 m isobath. The behavior of these waves
 895 depended on their amplitude: waves smaller than about 50 m and 100 MJ m⁻¹
 896 propagated adiabatically upslope with little change of form. Waves larger/more
 897 energetic than this formed packets via wave dispersion. Wave breaking was not
 898 observed at any time, with the possible exception of the largest wave that was
 899 steepening on the backside at the shallowest mooring, RPO at 266 m depth. The
 900 waves likely break, and/or reflect, inshore of 266 m where the bottom is also
 901 steeper. On the other hand, some of the b-waves were incident on YPO2 while
 902 others were absent at YPO2 and formed while the internal tide shoaled between
 903 YPO2 and RPO. These waves and wave packets were formed by the breaking of the
 904 leading, strongly convergent edge of the upslope-propagating internal tide (not to
 905 be confused with a breaking NLIW). This process took place near mooring CPO on

906 the 342 m isobath. This process occurred just once per day and was most easily
907 discerned by the downslope tidal current near the bottom which was not
908 complicated by upper ocean processes.

909
910 The energy transformations also depended on wave amplitude. For the smaller
911 waves ($E < 100 \text{ MJ m}^{-1}$), the incident APE was greater than the HKE and continued to
912 grow upslope. For the larger waves, the incident HKE was larger than the APE, but
913 the flux of HKE decreased sharply upslope especially between 342m to 266 m, while
914 the flux of APE in that depth range increased slightly, resulting in greater APE than
915 HKE farther onshore. These results are in rough agreement with recent theory and
916 numerical simulations of shoaling waves.

917
918 With the possible exception of one (largest) wave, no breaking NLIWs were
919 observed anywhere in the moored array. This is because neither of the criteria for
920 breaking waves was met: The orbital velocities never exceeded the propagation
921 speed, and wave amplitudes were too small. This situation contrasts with a similar
922 depth range farther southwest, where larger waves were already actively breaking
923 at the 300 m isobath. The more periodic, less turbulent environment presented to
924 the subaqueous sand dune field may be relevant to its formation location along the
925 slope. This and other forcing factors will be taken up in more detail in a subsequent
926 work.

927
928
929

930 **Acknowledgements**

931

932 This work was supported by the U.S. Office of Naval Research (ONR) under grant
933 N000141512464 and by the Taiwan Ministry of Science and Technology (MOST).
934 Wen-Hwa Her (IONTU) and Marla Stone (NPS) led the mooring work at sea. We
935 thank the officers and crew of the research vessels OCEAN RESEARCHER 1, OCEAN
936 RESEARCHER 3, and OCEAN RESEARCHER 5.

937

938

939

940 **References**

941

942 Alford, M. H., Lien, R.-C., Simmons, H., Klymak, J., Ramp, S. R., Yang, Y.-J., Tang, T.-Y.,
943 Farmer, D., and Chang, M.-H.: Speed and evolution of nonlinear internal waves
944 transiting the South China Sea, *J. Phys. Oceanogr.*, 40, 1338-1355, 2010.

945

946 Alford, M. H., MacKinnon, J. A., Nash, J. D., Simmons, H., Pickering, A., Klymak, J. M.,
947 Pinkel, R., Sun, O., Rainville, L., Musgrave, R., Beitzel, T., Fu, K.-H., and Lu, C.-W.:
948 Energy flux and Dissipation in Luzon Strait: Two tales of two ridges, *J. Phys.*
949 *Oceanogr.* 41, 2211-2222, 2011.

950

951 Alford, M. H., Peacock, T., and co-authors: The formation and fate of internal waves
952 in the South China Sea, *Nature*, 521, 65-69, 2015.

953

954 Buijsman, M. C., Kanarska, Y., and McWilliams, J. C.: On the generation and evolution
955 of nonlinear internal waves in the South China Sea, *J. Geophys. Res.-Oceans*, 115,
956 C02012, doi:10.1029/2009JC005275, 2010a.

957

958 Buijsman, M. C., McWilliams, J. C., and Jackson, C. R.: East-west asymmetry in
959 nonlinear internal waves from Luzon Strait, *J. Geophys. Res.-Oceans*, 115, C1057,
960 doi:10.1029/2009JC006004, 2010b.

961

962 Chang, M.-H., Lien, R.-C., Tang, T. Y., D'Asaro, E. A., and Yang, Y. J.: Energy flux on
963 nonlinear internal waves in the northern South China Sea, *Geophys. Res. Let.*, 33,
964 L03607, doi:10.1029/2005GL025196, 2006.

965

966 Chang, M.-H., Lien, R.-C., Lamb, K. G., and Diamessis, P. J.: Long-term observations of
967 shoaling internal solitary waves in the northern South China Sea, *J. Geophys. Res.-*
968 *Oceans*, 126, <https://doi.org/10.1029/2020JC017129>, 2021a.

969

970 Chang, M.-H., Cheng, Y.-H., Yang, Y.-J., Jan, S., Ramp, S. R., Reeder, D. B., Hseih, W.-T.,
971 Ko, D. S., Davis, K. A., Shao, H.-J., and Tseng, R.-S.: Direct measurements reveal
972 instabilities and turbulence within large amplitude internal solitary waves beneath
973 the ocean, *Communications Earth & Environments*, 2, doi:10.1038/S43247-020-
974 00083-6, 2021b.

975

976 Chen, Y.-J., Ko, D. S., and Shaw, P.-T.: The generation and propagation of internal
977 solitary waves in the South China Sea, *J. Geophys. Res.-Oceans*, 118, 6578-6589,
978 doi:10.1002/2013JC009319, 2013.

979

980 Chiu, L. Y. S., and Reeder, D. B.: Acoustic mode coupling due to subaqueous sand
981 dunes in the South China Sea, *J. Acoust. Soc. Am.*, 134, doi:10.1121/1.4812862, 2013.
982

983 Chiu, L. Y. S., Chang, A. Y. Y., and Reeder, D. B.: Resonant interaction of acoustic
984 waves with subaqueous bedforms: Sand dunes in the South China Sea, *J. Acoust. Soc.
985 Am.*, 138, doi:10.1121/1.4937746, 2015.
986

987 Du, T., Tseng, Y.-H., and Yan, X.-H.: Impacts of tidal currents and Kuroshio intrusion
988 on the generation of nonlinear internal waves in Luzon Strait, *J. Geophys. Res.-
989 Oceans*, 113, C08015, doi:10.1029/2007JC004294, 2008.
990

991 Duda, T. F., Lynch, J. F., Irish, J. D., Beardsley, R. C., Ramp, S. R., Chiu, C.-S., Tang,
992 T.-Y., and Yang, Y.-J.: Internal tide and nonlinear internal wave behavior at the
993 continental slope in the northern South China Sea, *IEEE/J. Oc. Eng.*, 29, 1105-
994 1131, 2004.
995

996 Egbert, G., and Erofeeva, S.: Efficient inverse modeling of barotropic ocean tides,
997 *J. Atmos. Oceanic Technol.*, 19, 183-204, 2002.
998

999 Farmer, D., Li, Q., and Park, J.-H.: Internal wave observations in the South China Sea:
1000 The role of rotation and non-linearity, *Atmosphere-Ocean*, 47, 267-280, 2009.
1001

1002 Farmer, D. M., Alford, M. H., Lien, R.-C., Yang, Y. J., Chang, M.-H., and Li, Q.: From
1003 Luzon Strait to Dongsha Plateau: Stages in the life of an internal wave,
1004 *Oceanography*, 24, 64-77, 2011.
1005

1006 Grimshaw, R., Pelinovsky, E. N., Talipova, T. G., and Kurkina, A.: Simulations of the
1007 transformation of internal solitary wave on oceanic shelves, *J. Phys. Oceanogr.*, 34,
1008 2774-2791, 2004.
1009

1010 Grimshaw, R., Guo, C., Helfrich, K., and Vlasenko, V.: Combined effect of rotation and
1011 topography on shoaling oceanic internal solitary waves, *J. Phys. Oceanogr.*, 44, 1116-
1012 1132, 2014.
1013

1014 Helfrich, K. R., and Melville, W. K.: On long nonlinear internal waves over slowly
1015 varying topography, *J. Fluid Mech.*, 149, 305-317, 1986.
1016

1017 Helfrich, K. R.: Internal solitary wave breaking and run-up on a uniform slope, *J.
1018 Fluid Mech.*, 243, 133-154, 1992.
1019

1020 Jackson, C. B.: An empirical model for estimating the geographic location of
1021 nonlinear internal solitary waves, *J. Atmos. Oceanic Technol.*, 26, 2243-2255, 2009.
1022
1023
1024

1025 Klymak, J. M., Pinkel, R., Liu, C.-T., Liu, A. K., and David, L.: Prototypical solitons in
1026 the South China Sea, *Geophys. Res. Lett.*, 33, L11607,
1027 doi:10.1029/2006GL025932, 2006.
1028

1029 Kunze, E., Rosenfeld, L. K., Carter, G. S, and Gregg, M. C.: Internal waves in
1030 Monterey Submarine Canyon, *J. Phys. Oceanogr.*, 32, 1890-1913, 2002.
1031

1032 Helfrich, K. R., Trowbridge, J. H., and Reeder, D. B.: High dissipation of an internal
1033 solitary wave over sand dunes, *J. Phys. Oceanogr.*, in review.
1034

1035 Hsu, M.-K., and Liu, A. K.: Nonlinear internal waves in the South China Sea, *Canadian*
1036 *Journal of Remote Sensing* 26, 72-81, 2000.
1037

1038 Lamb, K. G.: A numerical investigation of solitary internal waves with trapped
1039 cores formed via shoaling, *J. Fluid Mech.*, 451, 109-144, 2002.
1040

1041 Lamb, K. G., and Nguyen, V. T.: Calculating energy flux in internal solitary waves with
1042 an application to reflectance, *J. Phys. Oceanogr.*, 39, 559-580, 2009.
1043

1044 Lamb, K. G., and Warn-Varnas, A.: Two-dimensional numerical simulations of
1045 shoaling internal solitary waves at the ASIAEX site in the South China Sea, *Nonlin.*
1046 *Processes Geophys.*, 22, 289-312, 2015.
1047

1048 Lee, C. M, Kunze, E., Sanford, T. B., Nash, J. D., Merrifield, M. A., and Holloway, P.
1049 E.: Internal tides and turbulence along the 3000-m isobath of the Hawaiian
1050 Ridge, *J. Phys. Oceanogr.*, 36, 1165-1183, 2006.
1051

1052 Li, Q., and Farmer, D. M.: The generation and evolution of nonlinear internal
1053 waves in the deep basin of the South China Sea, *J. Phys. Oceanogr.*, 41, 1345-
1054 1363, 2011.
1055

1056 Lien, R. C., D'Asaro, E. A., Henyey, F., Chang, M. H., Tang, T. Y. and Yang, Y.-J.:
1057 Trapped core formation within a shoaling nonlinear internal wave, *J. Phys.*
1058 *Oceanogr.*, 42, 511-525 2012.
1059

1060 Lien, R. C., Henyey, F., Ma, B., and Yang, Y. J.: Large-amplitude internal solitary
1061 waves observed in the northern South China Sea: Properties and Energetics, *J.*
1062 *Phys. Oceanogr.*, 44, 1095-1115, 2014.
1063

1064 Liu, A. K., Ramp, S. R., Zhao, Y., and Tang, T. Y.: A case study of internal solitary wave
1065 propagation during ASIAEX 2001, *IEEE/J. Oc. Eng.*, 29, 1144-1156, 2004.
1066
1067

1068 Moum, J. N., Klymak, J. M., Nash, J. D., Perlin, A., and Smyth, W. D.: Energy
1069 transport by nonlinear internal waves, *J. Phys. Oceanogr.*, 37, 1968-1988, 2007.
1070

1071 Nash, J. D., Alford, M. H., and Kunze, E.: Estimating internal wave energy fluxes in the
1072 ocean, *J. Atm. and Oc. Tech.*, 22, 1551-1570, 2005.
1073

1074 Nash, J. D., Kunze, E., Lee, C. M., and Sanford, T. B.: Structure of the baroclinic tide
1075 generated at Kaena Ridge, Hawaii, *J. Phys. Oceanogr.*, 36, 1123-1135, 2006.
1076

1077 Nash, J. D., Kelly, S. M., Shroyer, E. L., Moum, J. N., and Duda, T. F.: The unpredictable
1078 nature of internal tides on the continental shelf, *J. Phys. Oceanogr.*, 42, 1981-2000,
1079 2012.
1080

1081 Orr, M. H., Mignerey, P. C.: Nonlinear internal waves in the South China Sea:
1082 Observations of the conversion of depression internal waves to elevation internal
1083 waves, *J. Geophys. Res.* 108, 3064, doi:10.1029/2001JC001163, 2003.
1084

1085 Ramp, S.R., Chiu, C. S., Kim, H.-R., Bahr, F. L., Tang, T.-Y., Yang, Y. J., Duda, T., and
1086 Liu, A. K.: Solitons in the Northeastern South China Sea Part I: Sources and
1087 Propagation Through Deep Water, *IEEE/J. Oc. Eng.*, 29, 1157-1181, 2004.
1088

1089 Ramp, S. R., Yang, Y. J., and Bahr, F. L.: Characterizing the nonlinear internal wave
1090 climate in the northeastern South China Sea, *Nonlin. Processes Geophys.*, 17, 481-
1091 498, doi:10.5194/npg-17-481-2010, 2010.
1092

1093 Ramp, S. R., Park, J.-H., Yang, Y. J., Bahr, F. L., and Jeon, C.: Latitudinal Structure of
1094 Solitons in the South China Sea, *J. Phys. Oceanogr.*, 49, 1747-1767, 2019.
1095

1096 Ramp, S. R., Yang, Y.-J., Jan, S., Chang, M.-H., Davis, K. A., Sinnett, G., Bahr, F. L.,
1097 Reeder, D. B., Ko, D. S., and Pawlak, G.: Solitary waves impinging on an isolated
1098 tropical reef: Arrival patterns and wave transformation under shoaling, *J. Geophys. Res.-*
1099 *Oceans*, in review.
1100

1101 Reeder, D. B., Ma, B., and Yang, Y. J.: Very large subaqueous sand dunes on the upper
1102 continental slope in the South China Sea generated by episodic, shoaling deep-water
1103 internal solitary waves, *Mar. Geol.*, 279, 12-18, 2011.
1104

1105 Rivera-Rosario, G., Diamessis, P. J., Lien, R.-C., Lamb, K. G., & Thomsen, G. N.:
1106 Formation of recirculating cores in convectively breaking internal solitary waves of
1107 depression shoaling over gentle slopes in the South China Sea, *J. Phys. Oceanogr.*, 50,
1108 1137–1157, <https://doi.org/10.1175/jpo-d-19-0036.1>, 2020
1109

1110 Scotti, A., Beardsley, R. C., and Butman, B.: On the interpretation of energy and
1111 energy fluxes of nonlinear internal waves: An example from Massachusetts Bay, J.
1112 Fluid Mech., 561, 103-112, 2006.
1113
1114 Small, J.: A nonlinear model of the shoaling and refraction of interfacial solitary
1115 waves in the ocean. Part I: Development of the model and investigations of the
1116 shoaling effect, J. Phys. Oceanogr., 31, 3163-3183, 2001.
1117
1118 Small, J.: A nonlinear model of the shoaling and refraction of interfacial solitary
1119 waves in the ocean. Part II: Oblique refraction across a continental slope and
1120 propagation over a seamount, J. Phys. Oceanogr., 31, 3184-3199, 2001.
1121
1122 Turkington, B., Eydeland, A., and Wang, S.: A computational method for solitary
1123 internal waves in a continuously stratified fluid, Stud. Appl. Maths., 85, 93-127,
1124 1991.
1125
1126 Vlasenko, V., Ostrovsky, V. L., and Hutter, K.: Adiabatic behavior of strongly
1127 nonlinear internal solitary waves in slope-shelf areas, J. Geophys. Res., 110, C04006,
1128 doi:10.1029/2004JC002705, 2005.
1129
1130 Vlasenko, V., Guo, C., and Stashchuk, N.: On the mechanism of A-type and B-type
1131 internal solitary wave generation in the northern South China Sea, Deep-Sea Res. I,
1132 69, 100-112, 2012.
1133
1134 Vlasenko, V., and Stashchuk, N.: Three-dimensional shoaling of large-amplitude
1135 internal waves, J. Geophys. Res.-Oceans, 112, C11018, doi:10.1029/2007JC004107,
1136 2007.
1137
1138 Vlasenko, V., and Hutter, K.: Numerical experiments on the breaking of solitary
1139 internal waves over a slope-shelf topography, J. Phys. Oceanogr., 32, 1779-1793,
1140 2002.
1141
1142 Yang, Y. J., Fang, Y. C., Chang, M.-H., Ramp, S. R., Kao, C.-C., and Tang, T.-Y.:
1143 Observations of second baroclinic mode internal solitary waves on the continental
1144 slope of the northern South China Sea, J. Geophys. Res.-Oceans, 114, C10003,
1145 doi:10.1029/2009JC005318, 2009.
1146
1147 Yang, Y. J., Fang, Y. C., Chang, Y.-T., Tang, T. Y., and Ramp, S. R.: Convex and concave
1148 types of second baroclinic mode internal solitary waves, Nonlin. Processes
1149 Geophys., 17, 605-614, doi:10.5194/npg-17-605-2010, 2010.
1150
1151 Zhang, Z., Fringer, O. B., and Ramp, S. R.: Three-dimensional, nonhydrostatic
1152 numerical simulation of nonlinear internal wave generation and propagation in the
1153 South China Sea, J. Geophys. Res.-Oceans, 116, C05022, doi:10.1029/2010JC006424,
1154 2011.
1155

1156
1157

APPENDIX A

Table 1. Mooring and Instrument Locations and Performance										
Mooring	Latitude (north)	Longitude (east)	Bottom Depth (m)	Instrument	Instrument Depth (m)	Start	Stop	Record Length (d)	Sample Interval (s)	Number of Points
RPO	21 53.334	117 33.676	266			6/1/14	6/18/14	18		
				★ADCP 300 kHz	31				90	17198
				★ADCP 300 kHz	105				90	17197
				★ADCP 300 kHz	190				90	17198
				SBE 37 (TSP)	27, 105, 184, 244			20	76354	
				SBE 39 (TP)	61, 91, 141, 170, 258			10	154792	
				SPE 56 (T)	45, 75, 125, 155, 199, 229			10	154794	
CPO	21 51.879	117 36.587	342			6/1/14	6/18/14	18		
				★ADCP 300 kHz	11				90	16394
				◆ADCP 300 kHz	263				90	16398
				★ADCP 300 kHz	269				90	16410
				SBE 37 (TSP)	43, 109, 169, 230, 307			10	148066	
				SBE 39 (TP)	78, 139, 200, 286			10	148066	
YPO1	21 49.998	117 37.600	372			6/2/14	6/19/14	18		
				✚ADCP 75 kHz	20				90	16537
				★ADCP 300 kHz	306				90	16537
				SBE 19 (TSP)	369		6/13/14	12	15	63517
				SBE 39 (TP)	35, 56, 92, 117, 178, 240			10	148845	
				SBE 39 (TP)	300		6/17/14	16	10	134727
				SBE 39 (TP)	354		6/10/14	9	10	70620
				SBE 56 (T)	76		6/8/14	7	10	54078
				SBE 56 (T)	147, 209, 270, 325			10	148845	
	Star Oddi (TP)	148, 188		6/11/14	10	10	77398			
YPO2	21 48.679	117 39.512	386			6/2/14	6/19/14	18		
				✚ADCP 75 kHz	20				90	16916
				★ADCP 300 kHz	301				90	16915
				SBE 39 (TP)	58, 97, 118, 180, 241			10	152252	
				SBE 39 (TP)	37, 354		6/17/14	10	133147	
	SBE 56 (T)	78, 149, 201, 272, 328			10	152252				
Source	21 52.630	117 37.128	328			6/1/14	6/18/14	18		
					SBE 37 (TSP)	26, 86, 147, 208, 268			10	142186
					SBE 39 (TP)	55, 116, 174, 238, 310			10	1142186
				★4-m bins down-looking, 30 pings per ensemble						
				◆4-m bins up-looking, 30 pings per ensemble						
				✚16-m bins down-looking, 10 pings per ensemble						

1158